On the topology of transported magnetic octupoles

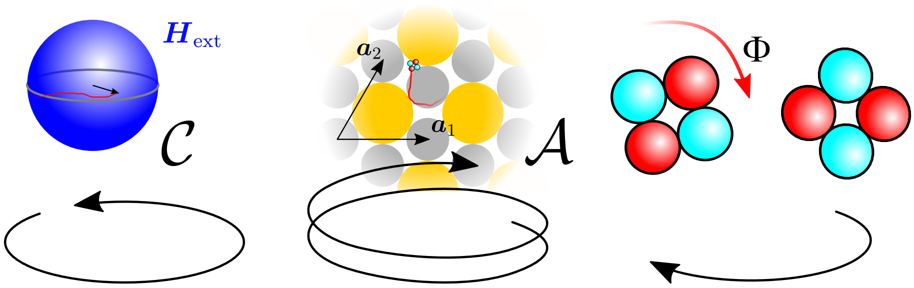

Masterarbeit aus dem Fachbereich Physik

der Universität Bayreuth

vorgelegt von

Thomas Lachner

Gutachter: Prof. Dr. Thomas Fischer
Lehrstuhl für Experimentalphysik X
Tag der Einreichung: 30. September 2019

Cover figure: Topological non-trivial behaviour of a free octupole. See figure 2.4 on page 18.

Abstract

Many physical systems are subjected to a large amount of perturbations and noise. Mathematical solutions might not be cast into a practical idea. Therefore, systems that are robust against perturbations gain high interest in current research. These systems extend from mesoscopic particle systems to microscopic quantum systems. A promising approach to robust response is the idea of topological protection. A quantity protected by some underlying topology cannot be disturbed by perturbations, that do not destroy the topology. Understanding such systems on several space and time scales is a fascinating field in physics. Research on topological physics gives possibilities to improve e.g. quantum computers or lab on a chip devices.

In this thesis the topological protected transport of free and that of locked induced octupoles is studied. The octupoles are placed on a magnetic pattern and driven by an external magnetic field. In this magnetic potential, build by the external and the pattern field, free octupoles, that were free to rotate, seek saddle point equivalent points. The topological protection in such a setup was studied in previous works with paramagnetic and diamagnetic particles seeking either maxima or minima of such a potential. Now, the non-trivial behaviour of points, equivalent to saddle-points can be studied.

Simple external field loops, consisting of merely precessing fields and polar orbiting fields, were used in the simulations to understand the movement of the free octupoles. Some sharp transitions of path types were found. These transitions were studied in detail and there was a better understanding in terms of exploring the parameter space close to the transition. The transition from trivial, contractable path loops towards non-trivial path loops with a winding number of two can be understood better by breaking the C_6 symmetry and studying the octupoles on a C_3 symmetric pattern.

Placing several free octupoles per unit cell gives the possibility to exchange two octupoles in a non-trivial way by winding them around each other. This braiding is of great interest for a topological quantum computer, where braiding is used to get topologically protected states.

Apart from free octupoles we further studied locked octupoles, where the orientation was locked at a fixed angle to the external field. Locked octupoles show a different behaviour, that can be explained based on the results of the free octupoles. In polar orbiting field loops, a sorting of locked octupoles with respect to their locking angle was observed. The locked octupoles were studied not only in simulations, but also in experiment. First results show promising features indicating the behaviour of locked octupoles.

Zusammenfassung

In vielen physikalischen Systemen spielt Rauschen eine große Rolle, besonders, wenn es darum geht, mathematische Modelle auf die physikalische Welt zu übertragen. In der aktuellen Forschung ist die Suche nach robusten Systemen aus diesem Grund von großer Bedeutung. Ein vielversprechender Ansatz ist der topologiche Schutz. Systeme, deren Eigenschaften topologisch geschützt sind, können nur durch äußere Einflüsse, die die Topologie zerstören, beeinflusst werden. Quantencomputer und Lab-on-a-chip-Anwendungen können somit deutlich verbessert werden.

In dieser Arbeit wird der topologisch geschützte Transport freier und versklavter, induzierter Oktupole untersucht. Die Oktupole werden auf ein magnetisches Muster gesetzt und von einem externen Magnetfeld angetrieben. In dem magnetischen Potential suchen die freien Oktupole, welche sich frei drehen können, Punkte, die topologisch äquivalent zu Sattelpunkte sind, auf. In vorangehenden Arbeiten wurde in solch einem System der topologisch geschützte Transport von Diamagneten und Paramagneten untersucht. Jene Teilchen suchen Minima und Maxima auf. Mit Oktupolen kann nun auf das nichttriviale Verhalten von Sattelpunkten eingegangen werden.

Das externe Feld wird dabei auf Bahnen bewegt, die sich aus präzessierenden Anteilen und polaren Orbits zusammensetzen. In den Simulationen mit freien Oktupolen wurden einige topologische Übergänge gefunden. Diese konnten besser verstanden werden, indem der Parameterbereich um die Übergänge untersucht wurde. So kann der Übergang von einem einfachen, zusammenziehbaren Pfad zu einem nicht-trivialen Pfad mit Windungszahl zwei erklärt werden, indem die Pfade auf Mustern, die lediglich eine C_3-, statt einer C_6-Symmetrie aufweisen, untersucht werden.

Mit mehreren freien Oktupolen pro Einheitszelle ist es möglich, diese umeinander zu winden und somit zu flechten. Dieses Themengebiet ist besonders im Bereich topologischer Quantencomputer relevant. Durch die Verflechtung von Quasiteilchen können topologisch geschützte Zustände für Quantencomputer erzeugt werden.

Neben freien Oktupolen wurden auch versklavte Oktupole untersucht, deren Orientierung mit einem beliebigem aber festem Differenzwinkel bezüglich des externen Feldes vorgegeben ist. Das abweichende Verhalten der verskavten gegenüber der freien Oktupole kann mit den Erkenntnissen über freie Oktupole erklärt werden. Versklavte Oktupole können mittels polarer Orbits des externen Feldes nach den jeweiligen Differenzwinkeln sortiert werden. Die versklavten Oktupole wurden sowohl durch Simulationen als auch in Experimenten erforscht. Erste Ergebnisse sind vielversprechend dahingehen, dass es sich bei den experimentell verwendeten Teilchen um versklavte Oktupole handelt.

Contents

1 Introduction 9

2 Theory 13
2.1 Topological protected transport 13
2.2 Braiding theory 18
2.3 Induced octupoles as saddle point seeking particles 21
2.4 Potential of free octupoles 22
2.5 Potential of locked octupoles 26
2.6 Pattern field for given symmetries 27

3 Simulations 29
3.1 Free octupoles 29
3.1.1 Precessing external field 30
3.1.2 Transport with polar orbits 37
3.1.3 Topological equivalence to saddle points 38
3.1.4 Pattern symmetries 41
3.2 Braiding with free octupoles 45
3.2.1 Exchange loop 47
3.2.2 Braiding loop 49
3.3 Locked octupoles 51
3.3.1 Path types for precessing fields 53
3.3.2 Sorting with polar orbits 58

4 Experiments 61
4.1 Setup and implementation 62
4.1.1 Goniometer 62
4.1.2 Probe chamber 63
4.1.3 Octupole particles 64
4.1.4 Precessing external fields 66
4.2 Results for locked octupoles 67

5 Conclusion 71
5.1 Summary of particle types and their behaviour 71
5.2 Outlook 74

A Programs in Python 75
A.1 Version, packages, and scripts 75

A.2 Particle forces 76

List of Symbols and Abbreviations **79**

List of Figures **81**

Bibliography **83**

1 Introduction

> As far as the laws of mathematics refer to reality, they are not certain; and as far as they are certain, they do not refer to reality.
>
> *(Albert Einstein)*

Many physical systems are difficult to understand, difficult to describe in a theoretical, mathematical way. For some of them good explanations exist, but nature does not know about this human-made theory and the results can only be taken qualitatively. One prominent case is the critical velocity of helium 4 (Zhu & Wu, 2015). Helium 4 is a superfluid and can therefore flow without friction up to a certain velocity, the critical velocity. Above the critical velocity, excitations are possible inside the fluid, leading to a dissipation of energy, so the fluid is no longer a superfluid. The phenomenon of the existence of the critical velocity is nicely described in theory, but the experimental values of the critical velocity are orders of magnitude smaller. This difference can not be explained. However, even in a theory with quantitative results, still many challenges arise by trying to control such a system in a precisely defined way. A lot of research is done directly or indirectly to gain or improve control over systems in the real world.

In many cases, the experimental realization is not equivalent to the quantitative theoretical model but contains perturbations that were neglected in the simple theory, but must be taken into account in the physical world. This is a huge problem in e.g. the field of quantum computation. The ideas of quantum computers were already present in the 1980s, the theory was then advanced by Shor (1994) and is quite established. Still, the realization faces many problems implementing devices with a larger amount of so called qubits. Qubits are the information saving unit, analogue to a bit in a classical computational device. The challenge of quantum computation is the stability and fault tolerance of the whole system.

However, not only the quantum world suffers from uncertainties, a lot of classical particle systems face these challenges, too. Classical systems are subjected to noise, induced by e.g. Brownian motion. However, a lot of applications demand a high precision control over micrometer sized particles: imagine a lab on a chip device working with tiny amounts of chemicals to analyse a sample rapidly, with high precision and without producing a lot of chemical waste; try to deliver a drug containing vesicle in a body and release the drug only in the infected region to avoid treating the whole organism. Repeatable and reliable control is necessary in all these classical systems over large time scales.

There are several approaches to face these challenges. A very promising one, covering several of the mentioned examples, is the use of topological protection. The basic idea is, that a topological quantity defines the state of the system. If a set of perturbations cannot affect the topology, then the topological quantity is an invariant under these perturbations and the state itself is protected.

An impressive example from solid state physics are topological insulators (Hasan & Kane, 2010). These materials are insulating in the bulk, therefore the Fermi energy is located in the band gap. A topological property of the band, the so called Chern number, distinguishes topological different bands. The Chern number is an invariant of the system, similar to the genus of a surface presented in section 2.1. The electron band in vacuum has a trivial band structure and zero Chern number, topological insulators have a non-trivial, non-zero Chern number. Connecting a topological insulator to e.g. vacuum leads to a closure of the gap at the surface of the material to cover for the difference in Chern number. Hence, conducting edge states exist due to the topology of the band. These edge states are furthermore protected against perturbations and inhomogeneities, as an electron on such an edge state cannot be scattered into a bulk state at the same energy level. The same underlying physics can be used to explain several transport behaviours in very different systems: Electrons or holes are transported along an edge in topological insulators; Gyroscopic waves travel without dispersion on a arbitrary shaped edge as described by Nash *et al.* (2015); Colloidal particles can be transported along an edge of the symmetry of the magnetic pattern they are placed on (Löhr *et al.*, 2018).

In quantum computation the usage of non-abelian anyons (further description in section 2.2) seems to be a promising idea (Nayak *et al.*, 2008). The non-trivial topological behaviour upon exchange of anyonic particles can be used to store information in topological protected qubits. This opens the field of topological quantum computation, where robustness is gained through an underlying topology.

In the classical field of high precision control over small particles, many solutions and ideas exist to deal with perturbations and noise. Micrometer sized magnetic particles can be transported by a simple, but well defined gradient field (magnetic tweezers). They can also be manipulated by rotating fields to form rolling clusters (Maier *et al.*, 2016) or propelling carpets (Martinez-Pedrero & Tierno, 2015) to be transported in a well defined direction at a certain speed. A drawback combining these methods is that all particles in the sample are treated equal and individual transport is a further challenge. Furthermore, optical tweezers and similar techniques create strong, local minima to trap single particles with forces orders of magnitudes stronger than the Brownian random forces. Moving the traps transports the particles. Dufresne & Grier (1998) describe how even several particles can be manipulated individually.

Löhr *et al.* (2016) found a method of using topological protection to guide magnetic particles along a magnetic pattern. The particles follow some potential minimum adiabatically and well defined by topological quantities. Thus, this approach combines both mentioned fields, topology and controlling small particles. A high precision is achieved as the transport is not dissipative and can be combined by an arbitrary control over the transport directions of both paramagnets and diamagnets individually. All particles of one type show precisely the same transport behaviour and individual transport is only possible for different particle types.

In this thesis, the topological protected transport of freely rotating and orientationally locked induced magnetic octupoles, placed on some magnetic pattern and driven by an external field will be investigated. The topological protection can be combined with an individual control over identical particles placed, in one unit cell, allowing for complex transport and braiding loops. Free and locked octupoles are interesting for both research areas, the anyonic braiding theories in quantum computation and multi-particle transport problems for various applications.

In chapter 2, the basics of topologically protected transport, as well as the motivation to use induced octupoles are presented. It will conclude that free octupoles are promising candidates to follow the non-trivial topology of points equivalent to saddle-points and can be used to perform a 2D braiding movement. In chapter 3, both particle types, free and locked octupoles are simulated using varying parameters to study their behaviour upon external, driving fields on pattern of different symmetries. The concepts of different ways of individual transport and braiding of free octupoles are demonstrated. In chapter 4, an experimental setup to study induced octupoles in the lab is presented, showing the basics of the distinct behaviour of locked octupoles.

2 Theory

In this chapter, the results of the work of Johannes Löhr on topological protected transport of magnetic particles is summarized. These results are the theoretical background of the ideas developed in this thesis. Furthermore the theory on braiding of particles and the theoretical thoughts on induced octupoles as suitable candidates for particles that seek saddle-point equivalent points are presented. Finally, the necessary forces and potentials manipulating free and locked induced magnetic octupole particles are calculated. This chapter thus proviedes the necessary toolbox for simulating and understanding the details of the dynamics of octupoles presented in chapter 3.

2.1 Topological protected transport

Topology is a mathematical field, describing properties of surfaces or other geometrical objects in space, that are invariant under continuous deformations. One of these quantities is the genus of a geometrical object, measuring the number of holes, independent of the specific shape. In figure 2.1 an ensemble of objects with different shapes and partly identical and partly differing genus are shown. Objects of the same genus can be deformed smoothly into each other and are therefore topologically the same. A cup can smoothly be deformed into a doughnut. To change the genus, the set of deformations has to include cutting or glueing, which is not considered a smooth deformation. Geometric objects, like the cup and the plate in figure 2.1, are topologically different.

If physical properties only depend on topological invariants, these properties are quite robust, as most smooth transformations do not change the underlying topological quantity and thereby the physical quantity remains unchanged. One of the topological invariants of a curve on a manifold is the winding number around a hole of the mathematical manifold $\mathcal{M}$. A periodic pattern can be described by a torus, by

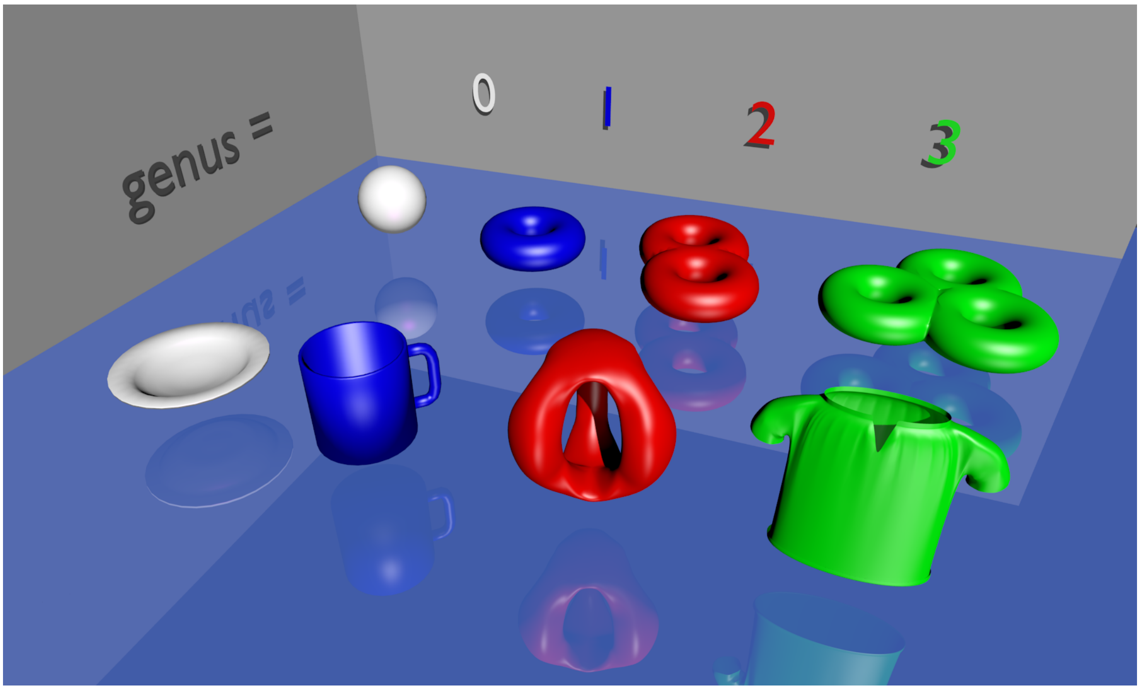

Figure 2.1: Geometrical objects having a different genus. Surfaces of equal colour are identical in a topological sense as they have the same genus. Sphere and deformed sphere (plate) have genus 0 (left, white). Torus and cup have genus 1 (blue). The red (green) surfaces have more holes, which corresponds to a genus of 2 (3).

glueing the opposite edges of one unit cell together. This transformation is shown in figure 2.2. Transport on periodic patterns can now be described by a set of winding numbers around either of the two holes of the torus.

Transport of a particle placed on a periodic pattern can be divided into the movement in one unit cell and the effective transport by one lattice vector of a position in one unit cell to the corresponding position in another unit cell. The second part of the transport corresponds to a non-zero winding number on the torus representing the periodic pattern. The 2D space of the pattern, on which the movement takes place, is called **action space** $\mathcal{A}$.

An external, driving field of constant strength has a parameter space, that can be described by a sphere. We call this space the **control space** $\mathcal{C}$. The driving shall adiabatically transport particles on $\mathcal{A}$, such that no transport occurs, if the driving field stops. A sphere has genus $g = 0$ which is shown in figure 2.1. Any loop on a sphere can therefore be deformed smoothly into a point. Hence, such loops are equivalent to a field that stays constant throughout time, which obviously cannot induce transport in the action space. We call any loop of the driving field $\mathcal{C}$-loop to

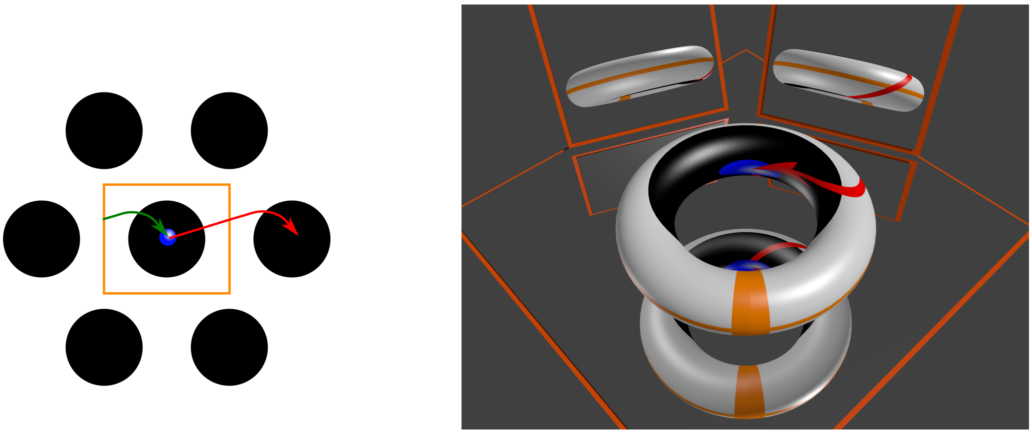

Figure 2.2: The sixfold pattern shown on the left can be represented as a torus, which is shown on the right. Only one unit cell (orange border) is mapped onto the surface of the torus by glueing the left to the right border and the top to the bottom border respectively. Due to periodicity, leaving the orange marked unit cell on the right boundary (indicated by the red arrow) is the same as entering the same, marked unit cell from the opposite side (green arrow). On the torus, a movement by one unit vector forms into a curve that has a non zero winding number W around one of the two holes. This is indicated by the red arrow on the torus representing a closed curve with $W = 1$.

distinguish them from path loops of the particles in $\mathcal{A}$.

Any closed $\mathcal{C}$-loop of a magnetic field that leads to transport on a periodic pattern is therefore topological distinct from one leading to no transport. This is a simple conclusion out of the fact, that this path must not be contractable to a point. If one observes transport, the sphere has special points, the **bifurcations points**, that puncture the control space. Encircling one of those points is different from a $\mathcal{C}$-loop without any bifurcation point inside. In figure 2.3, these bifurcation points are the tips of the fence in $\mathcal{C}$. Encircling some of the bifurcation points with an external field $\mathcal{C}$-loop can transport a particle in different directions.

In Löhr *et al.* (2016) the topological transport behaviour is shown in a set of magnetic, colloidal systems. The action space is a periodic magnetic structure giving rise to a pattern magnetic field $\boldsymbol{H}_{\mathrm{p}}$. The control space consists of all orientations of an external magnetic field but those pointing towards the previously mentioned bifurcation points. Hence, $\mathcal{C}$ is a punctuated sphere. Different symmetries of the pattern lead to differently punctuated control spaces and the curves of $\boldsymbol{H}_{\mathrm{ext}}$ can obtain different winding numbers. These winding numbers control the transport of para- or diamagnetic particles set on the pattern.

The colloidal potential $U \propto H^2$ is proportional to the square of the total magnetic field $\boldsymbol{H} = \boldsymbol{H}_{\text{ext}} + \boldsymbol{H}_{\text{p}}$. The external field is changed slow enough, such that the movement of a particle in $\mathcal{A}$ can stay adiabatic. The position of a particle is at any time given by an extremal point of this potential. Paramagnetic particles seek the maxima, whilst diamagnetic particles are located in minima positions. Knowing about the behaviour of the extrema therefore explains the movements of particles in the action space. The mathematical space to describe this is the span of the 2D action space and the 2D control space and is therefore 4D. The extrema form a 2D manifold $\mathcal{M}$ in this space $\mathcal{A} \otimes \mathcal{C}$, the topology can be visualized in 3D as shown in figure 2.3. These manifolds are topologically nontrivial objects with a certain number of holes. Non zero winding numbers of paths for a single type of extrema correspond to non zero winding numbers in $\mathcal{A}$ and hence transport of e.g. a paramagnet into one direction.

In a pattern with a 6 fold rotational symmetry, called C_6, $\mathcal{C}$ is divided into three sections as shown in figure 2.3. The regions are separated by the **fence**, that connects the bifurcation points. In the northern (southern) region, 2 minima (maxima) coexist with 1 maxima (minima) and 3 saddle points per unit cell. The tropics only contain 1 minima and maxima and 2 saddle points. By crossing the fence, whilst leaving the tropics, a pair of one saddle point and one minima (maxima) is created. Returning to the tropics, this pair vanishes again, leading to a possible ratchet transport of particles even if the driving frequency is slow. The ratchet occurs, when the particle sits in the disappearing minimum (maximum).

The manifold $\mathcal{M}$ is one connected surface of genus 7, as shown in figure 2.3. $\mathcal{M}$ can be split into 3 sub-manifolds for minima, maxima and saddle point. The saddle point region has genus 3, the others have genus 2. All of them provide a set of winding numbers, that can be used to explain the non trivial transport of particles into the next unit cell for a closed driving $\mathcal{C}$-loop.

In $\mathcal{A}$, the area can be split into sub-areas, accessible to both maxima and minima, and sub-areas accessible to saddle points only. This can be seen in figure 2.3. An opposite field in $\mathcal{C}$ renders the same point in $\mathcal{A}$ stationary, thereby changing role of positive and negative curvature. This converts minima into maxima and rotates saddle-points by $\pi/2$. The sub-areas are connected by a single point, the **gate**. The gates are special points in $\mathcal{A}$, that get stationary by a full grand circle in $\mathcal{C}$, shown in figure 2.3.

Choosing special $\mathcal{C}$-loops therefore leads to transport of minima, maxima or saddle points in $\mathcal{A}$. At least two of the extrema in $\mathcal{A}$ can be transported individually in

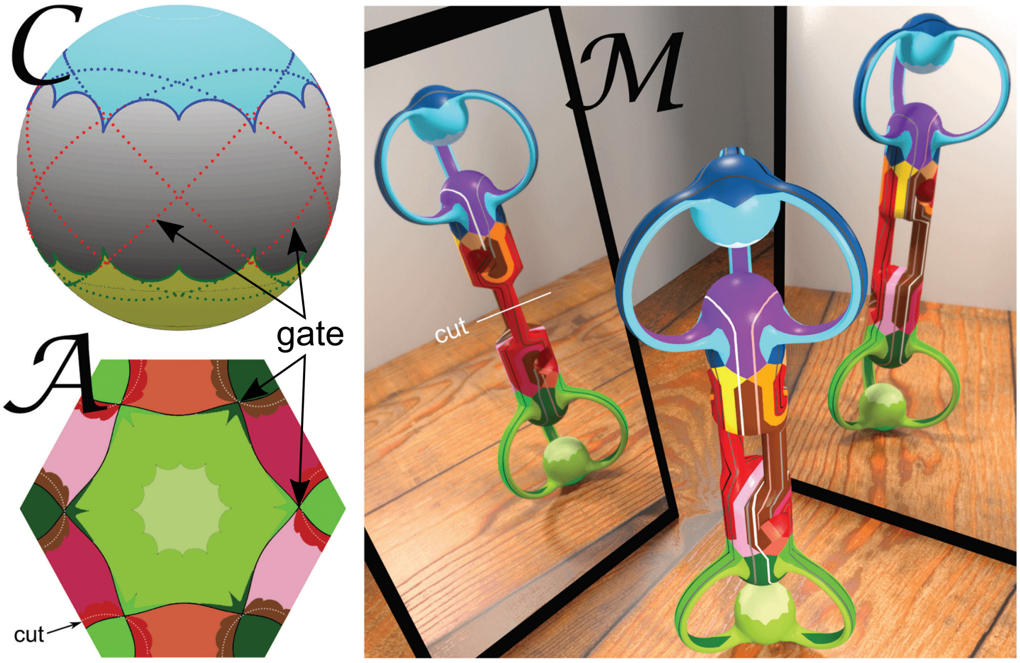

Figure 2.3: Controlspace $\mathcal{C}$, action space $\mathcal{A}$ and manifold $\mathcal{M}$ of a C_6 periodic pattern. The blue colours correspond to the minima areas, the green colours to the maxima and the red/purple colours to the saddle point areas. Diamagnetic particles go to minima, paramagnetic particles to maxima. In $\mathcal{C}$ an extra minimum (maximum)exists in the excess region in the north (south), always accompanied by an extra saddle point. The different shades of blue (green) indicate the minima (maxima) position in $\mathcal{A}$ and $\mathcal{M}$ that correspond to external fields pointing in different sub-areas of $\mathcal{C}$. Dark colours label the two extrema in the excess region in the north (south), light colours label the tropics and the south (north). In $\mathcal{A}$ only the the bottom half of $\mathcal{M}$ is mapped (indicated by the cut). In $\mathcal{C}$ the gates are grand circles with segments for minima, maxima and saddle points coloured respectively. In $\mathcal{A}$ the gates are points. Pictures from Löhr *et al.* (2017).

separate, independent directions. The saddle point region is different from the others, as the accessible region for external fields in the tropics forms a ring around a minima (maxima) sub-area. An external field $\mathcal{C}$-loop around the tropics of $\mathcal{C}$ crosses all 12 gate segments, 6 for each of the two saddle points existing in that area. However, the symmetry of the sub-area accessible to each saddle point is 3 fold. Hence, a saddle point driven by such a $\mathcal{C}$-loop has to move twice around the ring in $\mathcal{A}$. Therefore, a non-trivial behaviour is expected for an external field precessing around the equator. A saddle point travels 2π in $\mathcal{A}$, while the external field changes by π. The orientation of the saddle point itself changes by $\pi/2$, as both curvatures are exchanged. This behaviour is sketched in figure 2.4.

Furthermore the fact, that at least two saddle point positions exist in $\mathcal{A}$ for any

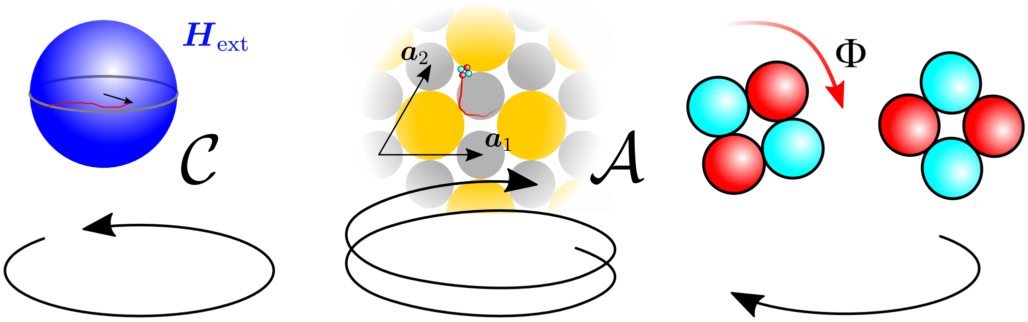

Figure 2.4: Expected non-trivial behaviour of a saddle point seeking particle. During one full external field $\mathcal{C}$-loop in the tropics (left) the particle will run twice around the interstitial points located above the small magnets (center) while its orientation Φ changes by π (right).

point in $\mathcal{C}$, excels these stationary points. Particles seeking a minimum (maximum) will always end up in the same position of one unit cell using arbitrary $\mathcal{C}$-loops. Manipulating multiple paramagnets or diamagnets differently with one driving $\mathcal{C}$-loop is generously not possible. In case of particles that seek the proximity of a saddle point, independent control of two particles is possible to a certain extend, as there are at least two distinct saddle points for arbitrary external field direction. In which position particles sit after leaving a minimum, maximum or saddle point, that vanished at the fence, is quite well understood from the topology of the underlying manifold in $\mathcal{M}$.

Finally, the idea of creating particles that are attracted by a saddle point itself is interesting, as physics is mainly determined by the maxima or minima of potentials. Combining these questions leads to the research presented in this thesis. In theory, simulations, and experiments, particles that seek stationary points topologically similar to saddle points, free octupoles, and the behaviour of these particles in driving, external fields are studied.

2.2 Braiding theory

As presented in section 2.1, the topologically protected transport of saddle points raises some interesting questions. Whereas minima and maxima in the described system behave quite similar, saddle points show a quite distinct behaviour. The main difference is that at least two saddle points exist in one unit cell at any time,

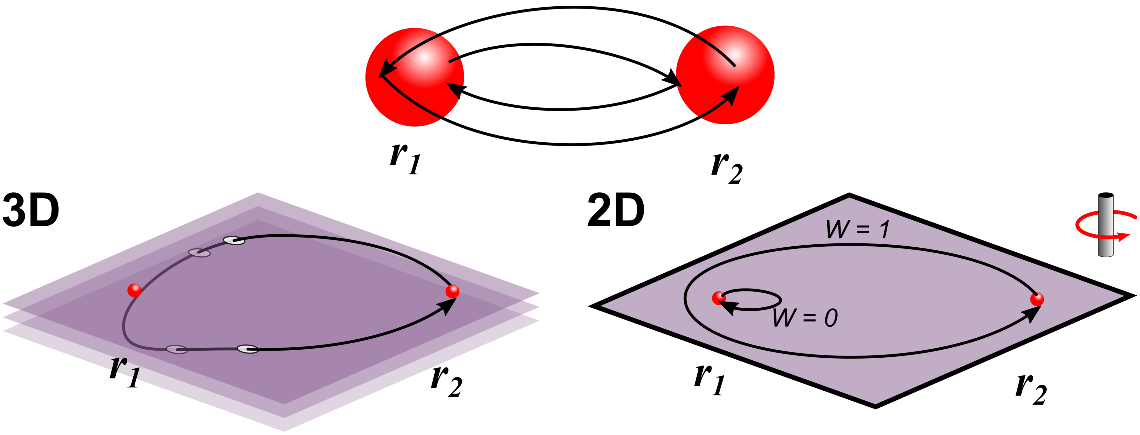

Figure 2.5: Exchanging two indistinguishable particles (red) twice, brings them back into their original position. This is equivalent to winding one particle around the other. Here the particle 2 starting at $\boldsymbol{r}_2$ is winding counter clockwise around the particle 1 sitting at $\boldsymbol{r}_1$. The path of particle 1 can be contracted to a point in any situation, as it is topologically equivalent to a point. The path of particle 2 can only be contracted in three spacial dimensions, as shown on the left. In two dimensions the path of particle 2 cannot cross the $\boldsymbol{r}_1$ location and cannot be deformed into a point. The winding number in this case is $W = 1$ for particle 2.

independent of the external field $\mathcal{C}$-loop. This opens new possibilities, as identical particles can now be manipulated independently, even if they are located in the same unit cell, rising some questions: Is it possible to exchange two particles in one unit cell? Can the exchange of the two saddle points change the topological state of the system?

The behaviour upon exchanging two particles defines the fundamental quantum statistics of fermions and bosons (Nayak *et al.*, 2008). If the particles are indistinguishable, the exchange can only change the phase α of the systems' wave function

$$\Psi(\boldsymbol{r}_2, \boldsymbol{r}_1) = e^{i\alpha}\Psi(\boldsymbol{r}_1, \boldsymbol{r}_2) \tag{2.1}$$

Exchanging indistinguishable particles a second time brings them back to their original position. Exchanging twice is analogue to winding one particle around the other as shown in figure 2.5. In three dimensions the winding of both particle can be contracted to a point, centred at its original and final position. Therefore no change happens in the system, hence the overall wave function has to be the same. But according to equation 2.1, a second phase shift occurs such that

$$\Psi(\boldsymbol{r}_1, \boldsymbol{r}_2) = e^{i\alpha}\Psi(\boldsymbol{r}_2, \boldsymbol{r}_1). \tag{2.2}$$

This can only be true for values of $\alpha = 0, \pi, ...$ The first case corresponds to bosons, the second to fermions such that the exchange of two particles is either symmetric (bosons) or antisymmetric (fermions).

However, in two dimensions the winding around another particle cannot be contracted without cutting the paths and glueing it back together as explained by Nayak *et al.* (2008). The topology of a path, that winds around another particle is different from trivial closed paths. Now any value for the phase α is allowed, as a system after winding one particle around the other is topologically different from the original system. This creates a new type of particles, that obeys a different quantum statistics. These particles are called **anyons**. The name refers to the phase α, that now can take **any** value.

As the winding can change the state of the system, one can imagine anyons as tips of a string in the time domain as shown in figure 2.6. These strings cannot intersect and hence a winding of the anyons is encoded in a braiding of these strings. In mathematics, taking n strings and the possible winding configurations form a group, the so called braiding group $\mathcal{B}_n$. The generators of the group elements σ_i with $1 \leq i \leq n-1$ describe the exchange of two neighbouring particles i and $i+1$. The inverse σ_i^{-1} exchanges them the way back whereas $\sigma_i \sigma_i \neq \mathbb{1}$ as the resulting braid has now a different topology although the particles sit in the same positions. The operations are obviously non-commutative, the braid group is therefore a non-abelian group. Braid elements are the same, if continuous deformations to the strings can bring them in the same configuration. Such deformations, that do not change the topology, are e.g. pulling at the ends of the strings or deforming a string.

The group theory of the braiding group combined with the anyon particles create interesting possibilities in the area of quantum computation. The main disadvantage of quantum computation is the error correction (Devitt *et al.*, 2013). Other than in classical systems, one can not proof read the quantum state containing the information, as this would destroy the state. It would be better to have a system, that is by itself quite protected against errors induced by perturbations. One such system is a system of non-abelian anyons as described in Nayak *et al.* (2008).

In solid state physics quasi-particles with anyonic behaviour can be found in quasi two dimensional systems. The electrons are strongly confined in one direction, still

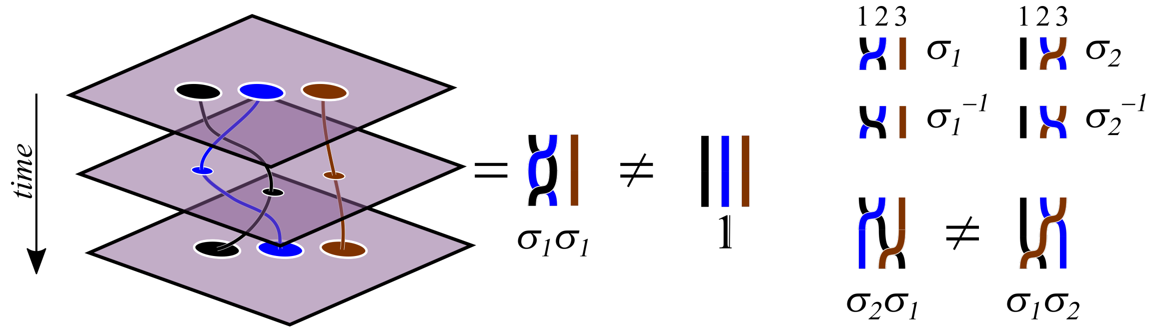

Figure 2.6: Three particles in two spacial and one time dimensions. The evolution of the particles' positions is shown as a string in the time domain. The left particles (black and blue) wind around each other, which can be described by the generator $\sigma_1\sigma_1$. This is obviously not equivalent to an undistorted system generated by a simple $\mathbb{1}$. The basic generators σ_1 and σ_2 and their inverse generators are shown in the right. The group generators do not commutate as illustrated above.

---

the electron stays a fermion. In such systems however, quasi-particles with anyonic characteristics can emerge. The most commonly known example, presented by Stern (2008), are the quasi-particles in the fractional quantum Hall effect. The filling factor ν is found to be a simple fraction $^m/_n$ with both m and n being integer numbers. The composite quasiparticle holds a fractional electron charge and a magnetic flux quantum. Those excitations are anyons and for special filling factors even non-abelian anyons.

2.3 Induced octupoles as saddle point seeking particles

In section 2.1 the idea of manipulating particles that behave like saddle points was introduced. It was motivated that particles that are attracted by a saddle point of some potential U show some interesting behaviour. In this section, an suggestion of creating such particles as free magnetic octupoles is presented.

A trivial, isotropic, symmetric particle cannot fulfil this requirement, as it's symmetry does not match the symmetries of the saddle point. A minimum or maximum can be described rotationally symmetric in a first approximation. In contrast to a minimum or maximum, a saddle point is characterized by different curvatures in the different directions, indicated by an indefinite Hessian matrix. This non-isotropic symmetry has to be considered when creating a particle, that seeks the vicinity of a saddle-point.

In a first approximation, the symmetry of a saddle-point is basically characterized by a switching of the curvature sign with each rotation of $\pi/2$. The change in the sign can be compensated by using two types of materials, that react effectively opposite in a given external field. Joining these materials in a "lucky clover" like arrangement can reproduce the symmetry of a saddle point, making it suitable to be attracted by saddle points.

In reality, this type of composite particle will rather seek the point of maximal difference of the eigenvalues of the Hessian matrix, as shown in section 2.4. For special cases, this can coincide with a saddle point, but generally these points are different. Nevertheless, for a slowly varying potential those positions should behave at least similar to a saddle point and can be considered topologically the same. This will be qualified in section 3.1.3.

If the external field is a magnetic field, an induced octupole can be realized by combining two diamagnets with two paramagnets. The external field induces a magnetic dipole in each individual particle, rendering an **induced octupole** in the composite particle, if the strength of all dipoles are exactly the same. If the strength do not balance, a dipole or quadrupole moment remains. Such an induced octupole is shown in figure 2.7. Apart from the position, induced octupoles have an additionally degree of freedom, the orientation. Two cases are studied here. Firstly, a particle, that can rotate freely, finding the right orientation depending on the given local structure of the potential. Secondly, the case of fixing the orientation to some external, induced direction.

In both cases, the octupoles are placed on top of a periodic, magnetic pattern and can be manipulated with an external magnetic field in analogy to the setup described in section 2.1. In the following sections, the potential and forces acting on an octupole and the magnetic field of the underlying pattern are derived.

2.4 Potential of free octupoles

In order to get the forces acting on the octupoles introduced in section 2.3 we need to calculate the magnetic potential for this particle type. Therefore knowledge on the magnetic field as well as on the composite particle geometry is necessary. In this section, the potential for a free octupole is derived. Further information on the pattern field is given in section 2.6.

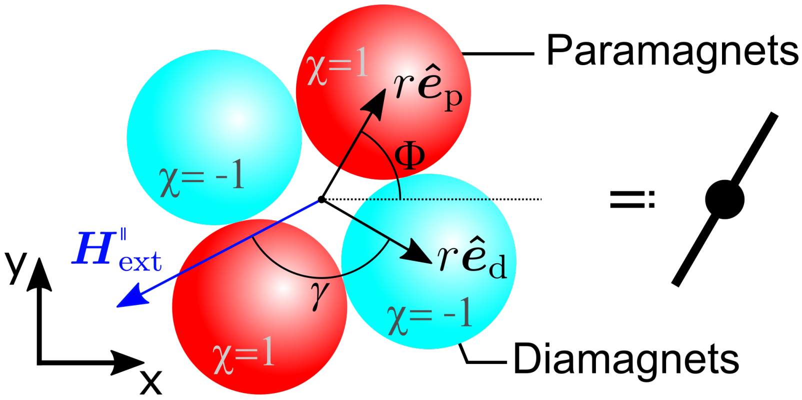

Figure 2.7: An induced magnetic octupole consists of two paramagnetic spheres (red) and two diamagnetic spheres (blue). The diamagnets can be e.g. superconducting spheres with $\chi = -1$, the paramagnets have then to be chosen oppositely. The angle Φ characterizes the orientation of the octupole in $\mathcal{A}$. The vector $r\hat{\boldsymbol{e}}_{\mathrm{p}}$ ($r\hat{\boldsymbol{e}}_{\mathrm{d}}$) gives the position of one paramagnet (diamagnet) relative to the center of the octupole. The projection of the external, driving field $\boldsymbol{H}_{\mathrm{ext}}$ into the x-y-plane is shown in blue. In the case of locked octupoles, the angle γ gives the locking towards the external field. A schematic picture, used in the later plots, is shown on the right. The dot gives the position of the octupole, the line indicates the direction of the paramagnets and therefore the orientation Φ.

The magnetic field in this setup consists of the external, driving magnetic field $\boldsymbol{H}_{\mathrm{ext}}$ and the pattern field $\boldsymbol{H}_{\mathrm{p}}$. The magnetization of induced magnetic particles is always parallel to the magnetic Field. It is given by

$$\boldsymbol{M} = \chi \boldsymbol{H} \tag{2.3}$$

where χ is the susceptibility of the material. The magnetic potential, calculated as the potential energy per volume, for such a particle is therefore given by

$$U_{\mathrm{magnetic}} = -\mu_0 \boldsymbol{H}\cdot\boldsymbol{M} = -\mu_0 \chi H^2 = -\mu_0\chi(\boldsymbol{H}_{\mathrm{ext}}\cdot\boldsymbol{H}_{\mathrm{ext}} + 2\boldsymbol{H}_{\mathrm{ext}}\cdot\boldsymbol{H}_{\mathrm{p}} + \boldsymbol{H}_{\mathrm{p}}\cdot\boldsymbol{H}_{\mathrm{p}}). \tag{2.4}$$

where μ_0 is the vacuum permeability. Integration over the particles volume gives the full magnetic energy, however, the particles are considered small compared to variations in the magnetic potential. Hence, the volume integration is neglected.

The external field is considered homogeneous throughout the sample, therefore $\boldsymbol{H}^2_{\mathrm{ext}}$ is a constant shift of the Potential U. Furthermore, the external field strength is considered strong compared to the pattern field, so that the last term in equation 2.4 can be neglected. In that case only the direction, not the magnitude of the external field is important for the driving of the particles. Combining these arguments, we can define a **universal potential**

$$U = \boldsymbol{H}_{\mathrm{ext}} \cdot \boldsymbol{H}_{\mathrm{p}}. \tag{2.5}$$

A paramagnet ($\chi_p > 0$) subjected to this potential maximizes U and a diamagnetic particle ($\chi_d < 0$) minimizes U by moving to another position, as the colloidal potential is

$$U_{\mathrm{colloid}} = \mu_0 \chi_{\mathrm{colloid}} U \tag{2.6}$$

The octupole, consisting of two paramagnetic particles and two diamagnetic particles as shown in figure 2.7, does not react to the potential itself, as both contributions cancel out in a first approximation. However, given the non-zero radius r of the particles, each particle will see a slightly different single colloid potential, such that the octupole potential is

$$\begin{aligned} U_{\mathrm{Octupole}}(\boldsymbol{x}) = & -\mu_0 \chi_p \left(U(\boldsymbol{x} + r\hat{\boldsymbol{e}}_{\mathrm{p}}) + U(\boldsymbol{x} - r\hat{\boldsymbol{e}}_{\mathrm{p}})\right) && (2.7) \\ & -\mu_0 \chi_d \left(U(\boldsymbol{x} + r\hat{\boldsymbol{e}}_{\mathrm{d}}) + U(\boldsymbol{x} - r\hat{\boldsymbol{e}}_{\mathrm{d}})\right) && (2.8) \end{aligned}$$

with $\hat{\boldsymbol{e}}_{\mathrm{p}}$ ($\hat{\boldsymbol{e}}_{\mathrm{d}}$) being a unit vector in the direction of one paramagnet (diamagnet). This can be simplified by implying that both particles have the same magnitude of magnetisation $\chi_d = -\chi_p$ and taking the maximal diamagnetic susceptibility $\chi_d = -1$. By adding a zero, this term can be brought in the following form:

$$\begin{aligned} U_{\mathrm{Octupole}}(\boldsymbol{x}) = \quad -\mu_0 r^2 \Bigg[& \frac{(U(\boldsymbol{x} + r\hat{\boldsymbol{e}}_{\mathrm{p}}) - U(\boldsymbol{x})) + (U(\boldsymbol{x} - r\hat{\boldsymbol{e}}_{\mathrm{p}}) - U(\boldsymbol{x}))}{r^2} \\ & - \frac{(U(\boldsymbol{x} + r\hat{\boldsymbol{e}}_{\mathrm{d}}) - U(\boldsymbol{x})) + (U(\boldsymbol{x} - r\hat{\boldsymbol{e}}_{\mathrm{d}}) - U(\boldsymbol{x}))}{r^2} \Bigg] \end{aligned} \tag{2.9}$$

which is for $r \to 0$ proportional to the second derivative of the universal potential evaluated in the directions of paramagnets and diamagnets respectively. Thus, the potential of an octupole rotated by the angle Φ relative to the x axis can be written as

$$U_{\mathrm{Octupole}}(\boldsymbol{x}, \Phi) = -\mu_0 r^2 \underline{\underline{\boldsymbol{t}}}(\Phi) : \nabla\nabla U(\boldsymbol{x}) \tag{2.10}$$

where $\underline{\underline{\boldsymbol{t}}}(\Phi)$ takes the orientation of para- and diamagnets into account. As the directions of both magnetizations are strictly orthogonal, we get

$$\underline{\underline{\boldsymbol{t}}}(\Phi) = \underline{\underline{\boldsymbol{R}}}(\Phi) \begin{pmatrix} 1 & 0 \\ 0 & -1 \end{pmatrix} \underline{\underline{\boldsymbol{R}}}^{\mathsf{T}}(\Phi) \tag{2.11}$$

with $\underline{\underline{\boldsymbol{R}}}(\Phi)$ being the 2D rotation matrix. The matrix entries $+1$ and -1 correspond to the directions of paramagnetic particles with $\chi = 1$ or diamagnetic particles with $\chi = -1$ respectively.

A **freely rotating octupole** will at every position minimize its energy by rotating around the z-axis. In this orientation, the paramagnets and diamagnets each are oriented along one eigenvector of the Hessian matrix. Instead of rotating the $\underline{\underline{\boldsymbol{t}}}$ matrix, $\nabla\nabla U$ can be replaced by its diagonalized form

$$\underline{\underline{\boldsymbol{R}}}^{\mathsf{T}}(\Phi_{min})\nabla\nabla U \underline{\underline{\boldsymbol{R}}}(\Phi_{min}) = \begin{pmatrix} \lambda_1 & 0 \\ 0 & \lambda_2 \end{pmatrix}, \tag{2.12}$$

which simplifies equation 2.10 as follows:

$$U_{\text{Octupole}}(\boldsymbol{x}) = -\mu_0 r^2 \begin{pmatrix} 1 & 0 \\ 0 & -1 \end{pmatrix} : \begin{pmatrix} \lambda_1(\boldsymbol{x}) & 0 \\ 0 & \lambda_2(\boldsymbol{x}) \end{pmatrix} = -\mu_0 r^2 \left(\lambda_1(\boldsymbol{x}) - \lambda_2(\boldsymbol{x})\right) \tag{2.13}$$

where λ_1 has to be the larger eigenvalue, as it is connected to the pair of paramagnets that tries to maximize the universal potential, leading to an overall negative octupole potential. $\lambda_{1,2}$ can be derived from the roots of the characteristic polynomial of the Hessian matrix of U.

$$\lambda_{1,2} = \frac{U_{xx} + U_{yy}}{2} \pm \sqrt{\frac{(U_{xx} + U_{yy})^2}{4} + U_{xy}^2 - U_{xx}U_{yy}} \tag{2.14}$$

where $U_{xx} = \partial_x \partial_x U$. A similar definition applies to U_{yy} and U_{xy}. Using equation 2.14 and equation 2.13, we get the expression for the minimal energy W of an octupole located at a certain position $\boldsymbol{x}$

$$W(\boldsymbol{x}) = -\mu_0 r^2 \left(\lambda_1 - \lambda_2\right) = -2\mu_0 r^2 \sqrt{\left(\frac{U_{xx} - U_{yy}}{2}\right)^2 + U_{xy}^2} \tag{2.15}$$

A freely rotating octupole in an universal potential $U(\boldsymbol{x})$ will seek the minima of $W(\boldsymbol{x})$, thus minimizing this energy leads to the positions of adiabatically driven free octupoles. The force acting on such an octupole is

$$\boldsymbol{F}_{\text{free}} = -\nabla W \tag{2.16}$$

and the orientation of the octupole is aligned with the eigenvectors $\hat{\boldsymbol{e}}_{\text{U}}^{1/2}$ of U

$$\hat{\boldsymbol{e}}_{\text{d}} = \hat{\boldsymbol{e}}_{\text{U}}^{2} \tag{2.17}$$

$$\hat{\boldsymbol{e}}_{\text{p}} = \hat{\boldsymbol{e}}_{\text{U}}^{1} \tag{2.18}$$

where $\hat{\boldsymbol{e}}_{\text{U}}^{1}$ belongs to the larger eigenvalue λ_1.

2.5 Potential of locked octupoles

A second type of induced octupoles emerges by locking the orientational degree of freedom. This is of interest as octupoles containing high temperature superconductors are used in chapter 4. The flux quanta penetrating those type-II-superconductors lock the orientation at a certain orientation towards the external field $\boldsymbol{H}_{\text{ext}}$. Thus the equations 2.15 - 2.18 cannot be used.

Locking the octupoles direction prohibits the rotation to find its minimal energy at each position $\boldsymbol{x}$. Up to equation 2.10, we have not used the rotational degree of freedom and can use this expression for the energy of a locked octupole for $r \to 0$. If we take the finite size of the octupole into account, it is easier to use equation 2.8. In the simulations, the force was derived by simply adding the forces acting on each sphere and applying it in the center of mass of the octupole. The torque on the octupole vanishes, when the angle between the external field and the orientation is locked to the initial angle, because the torsional constant from the flux quanta is orders of magnitude stronger than the magnetic torsional constant. The initial angle γ is kept constant throughout any field $\mathcal{C}$-loop. The strength of the torsional constant of the flux quanta legitimises the approximation that all forces act in the common center of mass. We can write the force on a locked octupole as

$$\boldsymbol{F}_{\text{locked}} = \chi_p \left(\boldsymbol{F}(\boldsymbol{x} + r\hat{\boldsymbol{e}}_{\text{p}}) + \boldsymbol{F}(\boldsymbol{x} - r\hat{\boldsymbol{e}}_{\text{p}})\right) + \chi_d \left(\boldsymbol{F}(\boldsymbol{x} + r\hat{\boldsymbol{e}}_{\text{d}}) + \boldsymbol{F}(\boldsymbol{x} - r\hat{\boldsymbol{e}}_{\text{d}})\right) \tag{2.19}$$

with $\boldsymbol{F}(\boldsymbol{x}) = \mu_0 \nabla U(\boldsymbol{x})$. The unit vectors $\hat{\boldsymbol{e}}_{\text{p}}$ and $\hat{\boldsymbol{e}}_{\text{d}}$ have to be determined by the fixed orientation of the octupole. The diamagnetic positions are rotated by an arbitrary, but fixed angle γ with regard to the external field projection, as sketched in figure 2.7. This type of locked octupoles will be studied in section 3.3 and in the experiments in chapter 4.

$$\hat{\boldsymbol{e}}_{\mathrm{d}} = \underline{\underline{\boldsymbol{R}}}(\gamma)\frac{\boldsymbol{H}_{\mathrm{ext}}}{H_{\mathrm{ext}}} \tag{2.20}$$

$$\hat{\boldsymbol{e}}_{\mathrm{p}} = \underline{\underline{\boldsymbol{R}}}(\frac{\pi}{2})\hat{\boldsymbol{e}}_{\mathrm{d}} \tag{2.21}$$

2.6 Pattern field for given symmetries

To describe the pattern, we must specify its symmetry and its lattice constant a. We can write the pattern field as Fourier series over the reciprocal lattice vectors of the periodic lattice. Let $q \approx 2\pi/a$ be the modulus of the smallest reciprocal lattice vector. The particles are located at an elevation $z > q^{-1}$ above the pattern, such that only the first Fourier components of $\boldsymbol{H}_{\mathrm{p}}$ are relevant. This elevations depends on the lattice constant a. Therefore, detailed information on the magnetic pattern itself is not necessary and opens the possibility to build these patterns in different ways, still getting comparable results, as long as the basic symmetries are respected.

As interesting changes appear for a six fold symmetric pattern, we start with a pure C_6 pattern. According to Löhr (2017), the pattern field gets decomposed into trigonometrical functions. The reciprocal lattice vectors of a two dimensional six fold pattern are

$$\boldsymbol{q}_i = \frac{2\pi}{a}\begin{pmatrix} -\sin(2\pi i/6) \\ \cos(2\pi i/3) \end{pmatrix} \tag{2.22}$$

for $i = 1, 2, 3$. The remaining component at high elevations at a given point $\boldsymbol{x}_{\mathcal{A}}$ in the action space is then proportional to

$$\boldsymbol{H}_{\mathrm{p}} \propto \sum_{i=1}^{3} \frac{2\pi}{a}\begin{pmatrix} -\sin(2\pi i/3)\sin(\boldsymbol{q}_i \cdot \boldsymbol{x}_{\mathcal{A}} + \phi) \\ \cos(2\pi i/3)\sin(\boldsymbol{q}_i \cdot \boldsymbol{x}_{\mathcal{A}} + \phi) \\ \cos(\boldsymbol{q}_i \cdot \boldsymbol{x}_{\mathcal{A}} + \phi) \end{pmatrix} \tag{2.23}$$

where ϕ is a parameter allowing a smooth change of the symmetry.

For a C_6 six fold symmetric pattern the extra phase vanishes, $\phi = 0$. An improper six fold symmetric pattern S_6, where a rotation by $\pi/3$ has to be combined with a mirror operator to retrieve a pattern symmetry, can be achieved by setting $\phi = \pi/6$. Values in between these extreme cases break the C_6 respectively S_6 symmetry to a lower C_3 three fold symmetry. Higher values of ϕ switch periodically between a C_6 and a S_6 pattern via all intermediate C_3 symmetries.

3 Simulations

We simulate the behaviour of octupoles placed on a magnetic pattern, such as the one shown on the left side of figure 3.1, as a function of the time dependent external driving field. The octupoles are simulated as individual Brownian particles. Interactions between the octupoles are neglected, as their induced fields are small compared to the potential inducing, external fields. As we are mostly interested in the paths of single octupoles, no hard core repulsion is introduced. The basic inputs of the python script, simulating the system, are particle types, starting positions and a stepwise defined driving $\mathcal{C}$-loop. The output data mainly consists of the position in $\mathcal{A}$ and orientation of the octupoles at each time step. Further information on the used scripts can be found in appendix A. All paths, observations, and conclusions in this chapter are based on the results from the simulations.

Section 3.1 will focus on the behaviour of free octupoles, being the most promising candidates to show the topologically characteristics equivalent to saddle points. A comparison to saddle points is included to show the topological equivalence of both. The exchange and the braiding of two or more free octupoles is examined in section 3.2. The different behaviour of locked octupoles, locked to the driving field direction, will be described and explained in section 3.3.

3.1 Free octupoles

The forces and potential of free octupoles were derived in chapter 2.4 (equations 2.15 - 2.18). In the center of figure 3.1, the potential landscape of a free octupole for an external magnetic field pointing north is depicted. We can spot tree distinct regions. The huge, central, yellow region **I0** above the central magnet is inaccessible to the octupoles but accessible to para- or diamagnets. The small yellow regions above the smaller magnets, the so called **interstitials**, are only accessible for fields close to the equator. However, the center of the interstitials cannot be reached in a C_6

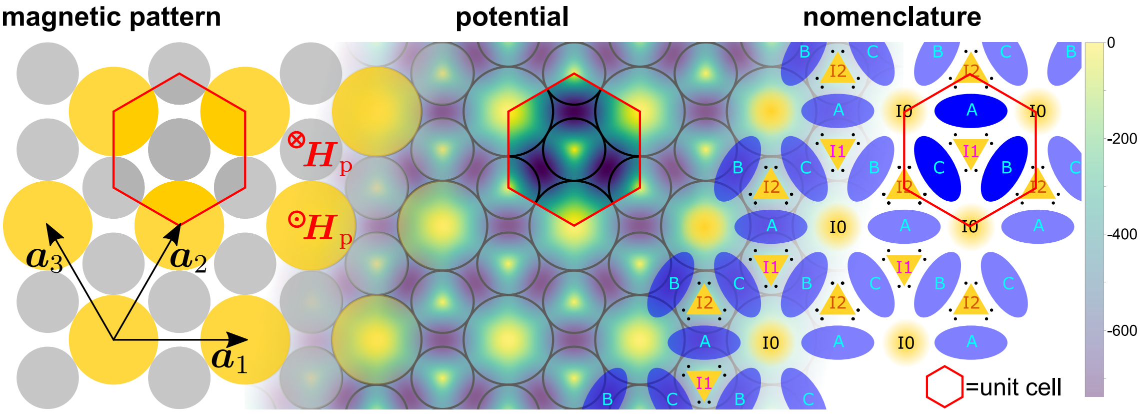

Figure 3.1: The sixfold pattern (C_6 symmetry) in different representations. From left to right: The pattern of neodymium magnets, as used in the experiments. The large, golden magnets are magnetized upwards, the smaller, silver ones are magnetized downwards. The coloured background in the center indicates the universal potential of a free octupole for an external field pointing up ($\theta = 0$). The colour bar on the very right relates the colours to arbitrary units, scaling the potential strength. Yellow colours are global maxima, blue colours global minima. On the right side distinguishable, special regions are sketched. The yellow triangles are the interstitials I1 and I2, the blue ellipses indicate the basins A, B, and C and the blurred yellow circle the region I0. In each representation, one unit cell is framed red. The black arrows indicate the primitive lattice vectors $\boldsymbol{a}_1$, $\boldsymbol{a}_2$, and $\boldsymbol{a}_3 = \boldsymbol{a}_2 - \boldsymbol{a}_1$.

---

symmetry. These areas are named **I1** and **I2**, as there are two of them per unit cell. The blue regions are the **basins**, containing the octupoles for a external field in the northern or southern hemisphere. The three distinct regions per unit cell are called **A**, **B**, and **C**. A scheme of these areas is shown in the right part of figure 3.1.

We will now simulate the behaviour of free octupoles in presence of an external, driving field. Therefore the loops of free octupoles, hence the paths of free octupoles in the action space $\mathcal{A}$ are studied. The octupoles are driven by some external magnetic field that moves on a $\mathcal{C}$-loop in the control space $\mathcal{C}$. First, only precessing fields are taken into account. Second, pure polar orbits are investigated. Third, the equivalence to saddle points is shown and the pattern symmetry is changed from C_6 to S_6.

3.1.1 Precessing external field

In figure 2.4 an non-trivial response of a free octupole to an external field running around the equator is predicted. In order to study this phenomena, the paths of free octupoles driven by a precessing external field $\boldsymbol{H}_{\text{ext}}$ are examined. As the field strength does not matter, the external field is defined by a fixed precession angle θ and the phase $\varphi(t)$, which varies with time. Starting from the north pole, θ is varied stepwise to study the different octupole paths at different, fixed values of θ. After a full $\mathcal{C}$-loop, the external field points in the same direction again, $\Delta\varphi = 2\pi$. Two kind of loops, trivial basin loops and non-trivial interstitial loops are observed. In this section, both observed loop types, as well as an analyses on the speed during these loops are presented.

Topologically trivial basins

For $\theta < \theta_c = 80.85°$ the octupoles run in a closed **basin loop** around one of the basins **A**, **B** or **C**. The radius of the loop in $\mathcal{A}$ changes with larger values of θ in the $\mathcal{C}$-loop. Furthermore, the shape of the loop differs more and more from a symmetric, circular path. Some exemplary loops in $\mathcal{A}$, as well as the orientations of the octupoles for different precession angles θ of the driving field are shown in figure 3.2.

The orientation of a free octupole during one of these cycles stays approximately the same and depends on the chosen basin. The paramagnetic particles within the octupole always point towards the large, central area, whilst the diamagnets are oriented towards the interstitials. Paramagnets and diamagnets switch role for fields precessing below the equator, leading to an effective rotation of $\Delta\Phi = \pi/2$ of one octupole, when comparing it to its orientation for fields in the other hemisphere. Furthermore, the positions in the basins change by a loop's phase π in $\mathcal{A}$, leading to opposite positions for same external phases $\varphi(t)$. This phase is assigned analogue to the colour assigned in the figure 3.2. For a reversed external field, the minimum position of an octupole coincides with the non-reversed minimum position, however with a $\pi/2$ change of orientation.

The relative orientation between two octupoles in two independent basins is $\Delta\Phi = \pm\,\pi/3$, if the two basins have different indices **A**, **B** or **C**. The position in the basins is correlated to the phase $\varphi(t)$ of the driving field, such that all octupoles are e.g. on the right, if the field points right (left) for fields in the northern (southern) hemisphere. This leads to different starting points in the various basins in relation to the individual surrounding which can be seen in figure 3.2 by comparing the color coding of the different loops.

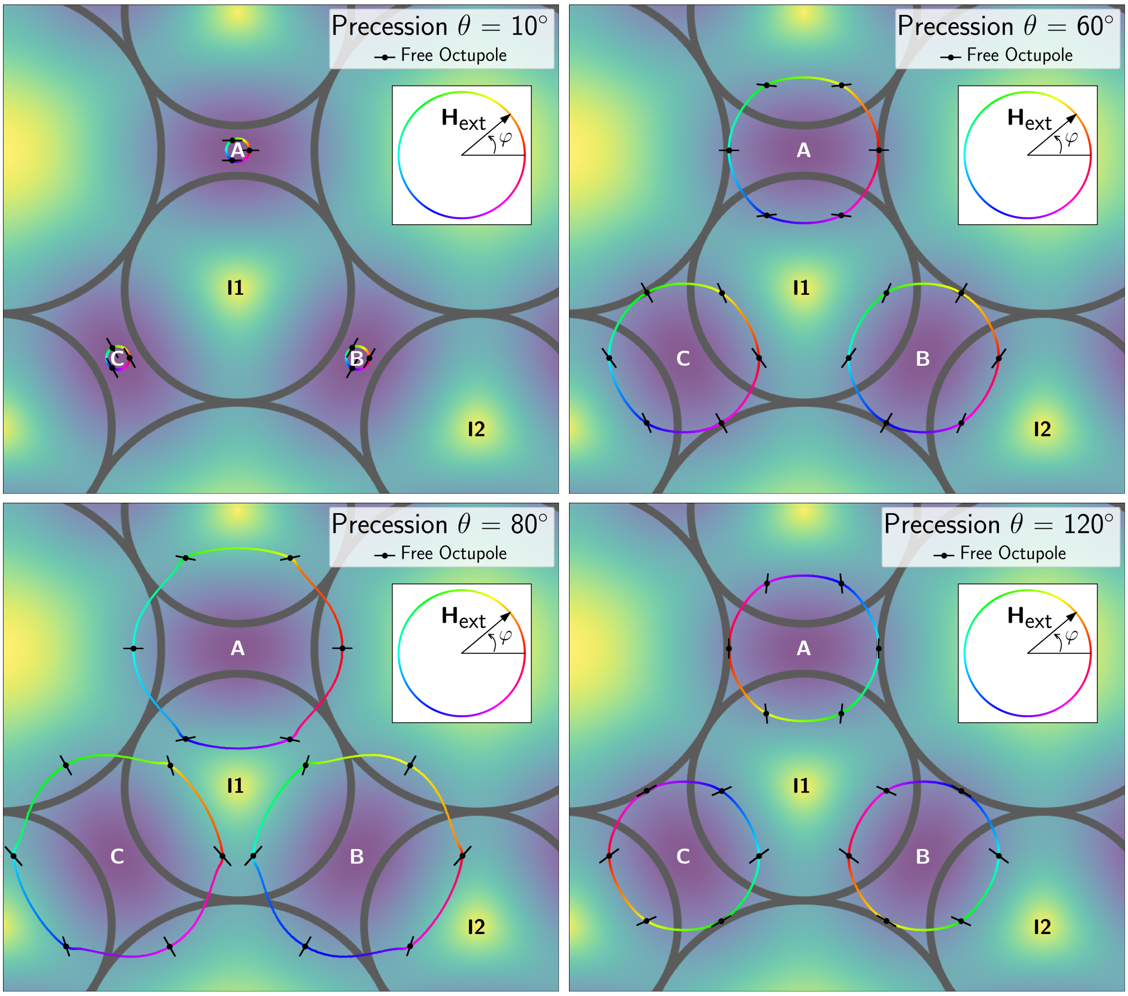

Figure 3.2: Paths for different precession angles, leading to closed **basin loops** in the basins A, B, and C. The colour of each path is changing according to the external field direction, as indicated in the insets. The field is rotating in a positive sense. At equally distanced times, the octupole is indicated by the black symbol, giving insight to its orientation. The octupoles in different basins are oriented with a relative orientation of $\pi/3$, the orientation itself stays almost constant during one loop. For precession angles θ closer to the equator of $\mathcal{C}$, the path is slightly deformed and deviates from a circle (bottom left). An equivalent $\mathcal{C}$-loop in the southern hemisphere (bottom right as compared to top right) rotates the free octupoles by $\pi/2$ and leads to a position in the loop in $\mathcal{A}$ that is shifted by a relative phase of the loop of π. This loop's phase is assigned to the position of some octupole on a given path, analogue to the colour in this figure. The size of the area included in one path depends heavily on the precession angle. Close to the poles the size decreases to a point (upper left).

Topologically non-trivial interstitial loops

Driving $\mathcal{C}$-loops with a precession angle closer to the equator $\theta_c < \theta < \pi - \theta_c$ lead to a **topological transition** of the loops in action space. The octupoles do not run around the basins any more, but run around one of the interstitials in a non-trivial way. In figure 3.3 such trajectories **double-triangle loops** are shown. During one cycle of 2π of the external field the octupoles encircle one of the two interstitials **I1** or **I2** twice. The winding occurs in the opposite direction compared to the external field direction. We can assign the driving $\mathcal{C}$-loop a winding number of $W_{\mathcal{C}} = 1$. The path loop then has a winding number $W = -2$. The path loop is split into six subsegments meeting in the turning points. There are two types of segments, one closer to the interstitial and one further away, leading to a kind of double-triangle-shape. The two types of segments are alternating during one cycle of the driving field. For $\theta = 90°$ the segments collapse and a single path, the **triangle loop**, remains as shown in the bottom left of figure 3.3.

A non-trivial precessing field $\mathcal{C}$-loop $\theta_c < \theta < \pi - \theta_c$ rotates the octupole by π. On each segment, the octupole is rotated by $\pi/6$, which leads to an orientation rotated by $\pi/2$ after the octupole encircled the interstitial once. The two collapsed positions for $\theta = 90°$ are therefore distinguishable by the orientation Φ of the octupole. Two octupoles on different interstitials I1 and I2 have a relative orientation of $\pi/2$. If we assign a phase to the position in one of the path loops (analogue to the colour in figure 3.3), the octupole in the other has a relative phase shift of approximately π (the path has to be rotated by 180° to be comparable). Hence when e.g. on I1 the octupole is on a fast, inner, ratchet like segment, the octupole on I2 is on a slow, outer, adiabatic segment. Due to the ratchet the phase shift is varying slightly from π.

As the interstitial points in the center of the small magnets itself cannot be reached, the winding is topologically different from the loops around the basins, that can contract to a point for the external field parallel to the z-direction. The described behaviour is topologically non-trivial as expected from the theoretical thoughts in section 2.1.

For $\theta > 90°$ the collapsed segments of the triangle loop split in a symmetric way to another double-triangle loop. The former inner paths are now the outer ones and vice versa. Increasing the precession angle further towards the south pole leads to a equivalent topological transition at $\theta = \pi - \theta_c$ towards the closed, trivial basin loops

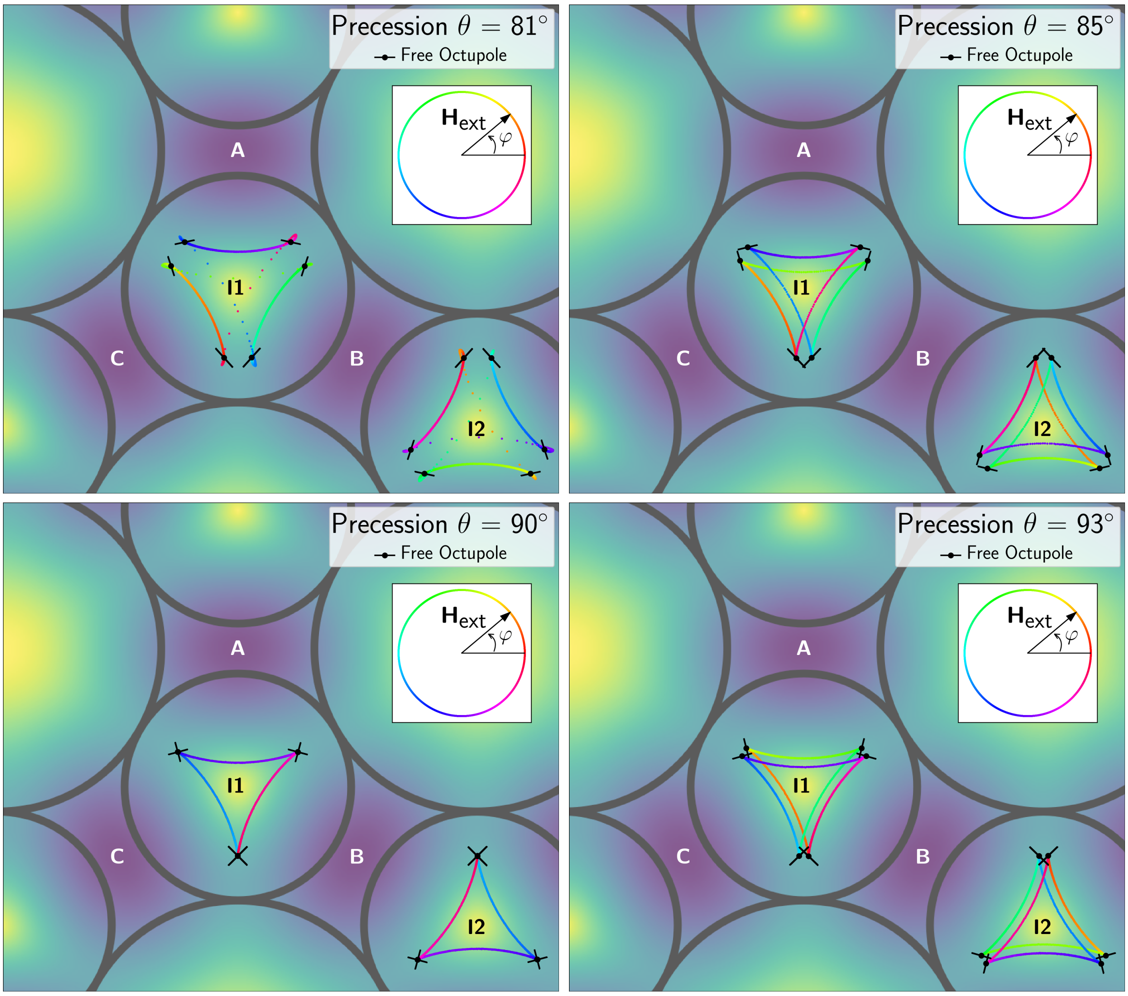

Figure 3.3: Paths for different precession angles of the driving $\mathcal{C}$-loop leading to non-trivial loops around the interstitials. The driving occurs in a positive sense. The octupoles at different interstitials are oriented with a relative orientation of approximately $\pi/2$ at any time. The orientation changes by π for one full cycle of the external field. Close to the transition $\theta \approx \theta_c$ to the basin loop of figure 3.2 a fast ratchet occurs (top left). A similar paths in the southern hemisphere leads to similar orientations but a position in the loop that is shifted by π (bottom right). The closer the precessing field is to the equator, the narrower is the gap between the paths segments. For a precession on the equator of $\mathcal{C}$, the two path segments collapse (bottom left) and form a **triangle loop**. The other cases show **double-triangle loops**. The colour of each path is changing according to the external field direction, as indicated in the insets. The black octupole symbols give insight into the octupole's orientation at certain, equally spaced time steps.

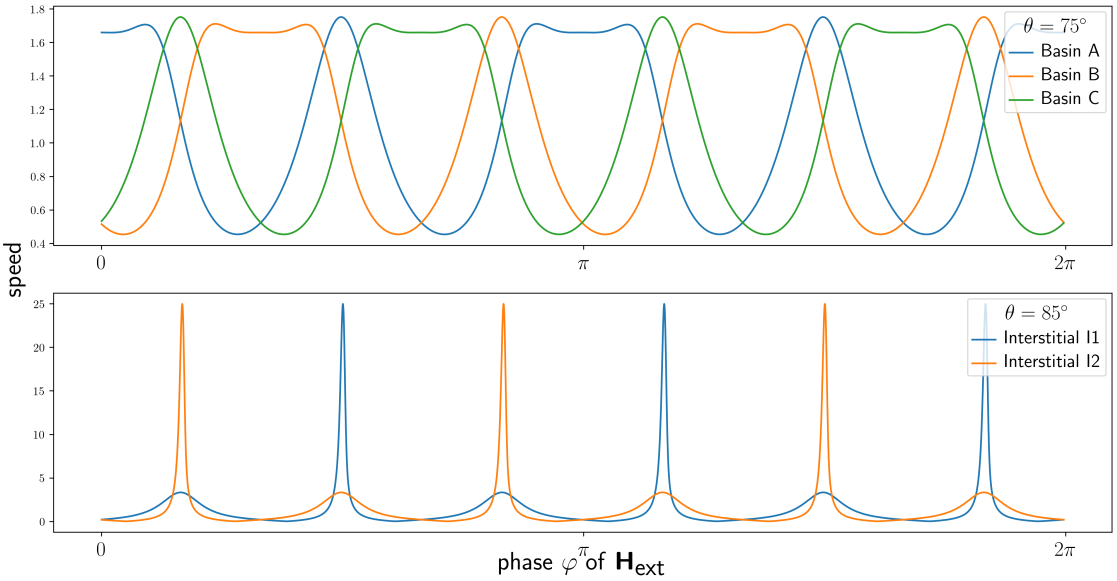

Figure 3.4: Speed of the octupoles during one external field $\mathcal{C}$-loop. For an octupole running around one of the basins (**upper plot**), four deep minima separated by a minor maximum and a plateau can be seen. The phase shift between two basins is $\pi/3$. For the loops around an interstitial point (**bottom**) six minima exist, separated by three major and three minor maxima, each corresponding to one of the six segments of the path. The positions of the minor maxima in the basins case correspond to the minor maxima in the interstitial case, the major maxima are slightly shifted in positive time direction, indicating a ratchet transition.

in one of the basins with orientations shifted by $\Delta\Phi = \pi/2$ as described above.

Paths velocity

The velocity throughout the described paths is not constant, which can be seen in figure 3.4. There are points in $\mathcal{A}$, where the octupoles are slower or even stop. Those **waiting positions** are located at each turning point separating the three faster segments from the three slower ones on the double-triangle loops around the interstitials. If θ gets closer to the poles, these positions travel on a circular path towards the basins in $\mathcal{A}$. On basin loops the octupoles do not stop at some corner. Still, the waiting positions are clearly visible in the speed plot 3.4, splitting each path into four segments. Connecting these points creates a line to the center of the basin in $\mathcal{A}$.

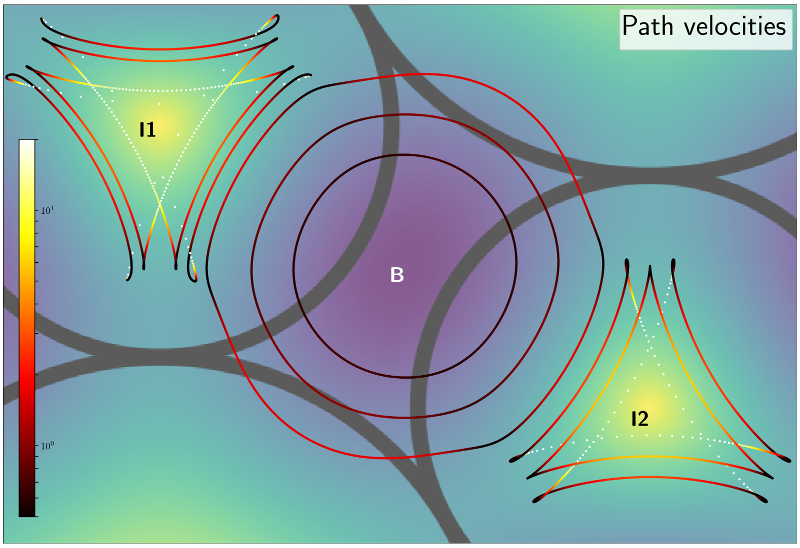

Figure 3.5: Paths for different values of θ coloured with the local speed of the octupole. Around I1 for precession angles 81° and 85°, around I2 83° and 90°, and around B 75°, 60°, and 45° (from outside to inside). The transition towards a transport around one interstitial occurs by connecting two slow parts of the basin loop with a fast ratchet. Interstitial loops close to the transition angle show a slight asymmetry in direction of the driving field.

Transition

The topological transition from the movement around the basins to the winding around the interstitials occurs via ratchets, combining loop segments of different basin loops to a double-triangle loop around the interstitial. This can be seen in figure 3.5. The segments, that used to be the slower segments in a basin loop, remain as the slower, outer segments of the double-triangle. At the end of such a segment on a double-triangle loop, an octupole can no longer follow the path of the former trival basin loop, but jumps to another stable position via a ratchet. For angles shortly after the transition, the path is clearly asymmetric, as the octupole tries to follow the basin loop for a short while, until the ratchet transition takes place. This asymmetry gets smaller for precession angles closer to the equator and vanishes for the triangle loop at $\theta = 90°$.

A ratchet itself is not time reversal, due to the fact, that the octupoles no longer adiabatically follow some minimum but slide on the path of steepest decent. An inverse field $\mathcal{C}$-loop can not push the octupole up the same way it slid down. Therefore, changing the direction of the external field changes the asymmetry. This breaking of symmetry is a clear sign that the described transition actually is a ratchet.

The transition can also be seen in the plot 3.4, as the small maxima are located at the same position, whereas the positions of the large maxima, describing the ratchets, are slightly shifted in positive time direction. Reversing the time changes the position of the ratchet jump. Furthermore, the speed on the slower segments stays comparable, whereas the speed on a ratchet close to the transition is orders of magnitude higher. Apart from that, a ratchet is characterized by a velocity almost independent on the driving frequencies, which correlates to the picture of a particle sliding down a slope until it can be transported adiabatically again.

The ratchet vanishes for $\theta = 90°$ on the equator due to symmetry. The role of adiabatic and ratchet segments of the double-triangle loop interchanges at this precession angle and only adiabatic segments exist in a triangle-loop.

3.1.2 Transport with polar orbits

Apart from simple precessing fields, another group of simple external field modulations is the group of polar orbiting grand circles. They are characterized by the azimuthal angle φ of the $\mathcal{C}$-loop, measured with respect to the lattice vector $\boldsymbol{a}_1$ and a varying polar angle $\theta(t)$. A combination of polar orbit segments and precessing fields can be used to design arbitrary $\mathcal{C}$-loops. In this section, the simulation results of octupoles driven by polar orbiting field $\mathcal{C}$-loops are presented.

As shown in section 3.1.1 the octupoles remain in the basins for external fields close to the poles. They remain in the space around an interstitial for external fields close to the equator. On a polar orbit, both regions are visited alternatingly, leading to a transport into neighbouring basins which is shown in figure 3.6. The azimuthal angle determines the transport direction. As transport only occurs along the primitive unit vectors, a stepwise transition separates these direction. If the external field rotates in a direction parallel to a unit vector, the paths are a straight connection into the neighbouring basins. Deviations from these orientations lead to more curved tracks through the action space.

As only two different interstitials exist, maximal two individual octupoles can be transported separately. The third basin, if filled at the beginning, is emptied with crossing the tropics for the first time. It can not go back, as it is emptied with a non reversal ratchet. This behaviour can be seen in figure 3.6. For $\varphi \in]-30°, 30°[$ basin A is emptied, for $\varphi \in]30°, 90°[$ basin B, basin C respectively continued. The transition of the transport direction correlates with a transition of basin stability.

These transition angles are separated by 60° due to the pattern symmetry and occur for fields aligned with the reciprocal lattice vectors $\varphi = 30°, 90°, \dots$, hence in between the primitive lattice vectors. Parallel to the primitive lattice vectors $\varphi = 0°, 60°, \dots$ another transition occurs. The direction of the first ratchet of an unstable basin changes direction (compare ratchet jumps from basin B in the lower row of figure 3.6). Along such a direction this jump is not topologically protected and an equal probability for both directions exists.

The two octupoles in the stable basins follow each other with a loop's phase shift of π and have a relative orientation of $\pi/2$. The orientation of one octupole slightly varies during one $\mathcal{C}$-loop, but does not fully rotate the octupoles, such that no net phase is accumulated along these paths.

Transport of octupoles in different directions can be archieved with more complex $\mathcal{C}$-loops. In section 3.2 this will be discussed in more detail.

3.1.3 Topological equivalence to saddle points

In section 2.3 free octupoles were motivated as particles with a topological behaviour similar to saddle-points. This assumption can further be verified by comparing the simulation results of free octupoles to the path data of a saddle-point. In this section the topological equivalence of octupoles and saddle-point-seeking particles will be shown by comparing the particle loops obtained by precessing external fields.

When calculating the position of a saddle point of U at each phase of the external, driving field, a path loop of a theoretically saddle point seeking particle, following a saddle point, is retrieved. In figure 3.7 such paths of saddle points, together with paths of free octupoles are shown. The equivalence to saddle points in a strict sense only exists for precession angles close to the poles. For other angles the paths deviate in form, still they intersect at six points. These points exist when the projection of the external field is aligned with the direction of one of the primitive lattice vectors of the pattern. That means the projection of $\boldsymbol{H}_{\mathrm{ext}}$ in the x-y-plane is parallel to some $\boldsymbol{a}_i$. However, topologically speaking, both paths are the same as both wind around the basins once per 2π of the external field. Even the orientations are aligned throughout the external field $\mathcal{C}$-loop.

In Löhr *et al.* (2016) the fence, at which the topological transition takes place, is found in the vicinity of $\theta = 60°$. As the octupoles have a transition angle of $\theta = 80.85°$ a region exists, where both particles, the octupole and the saddle-point

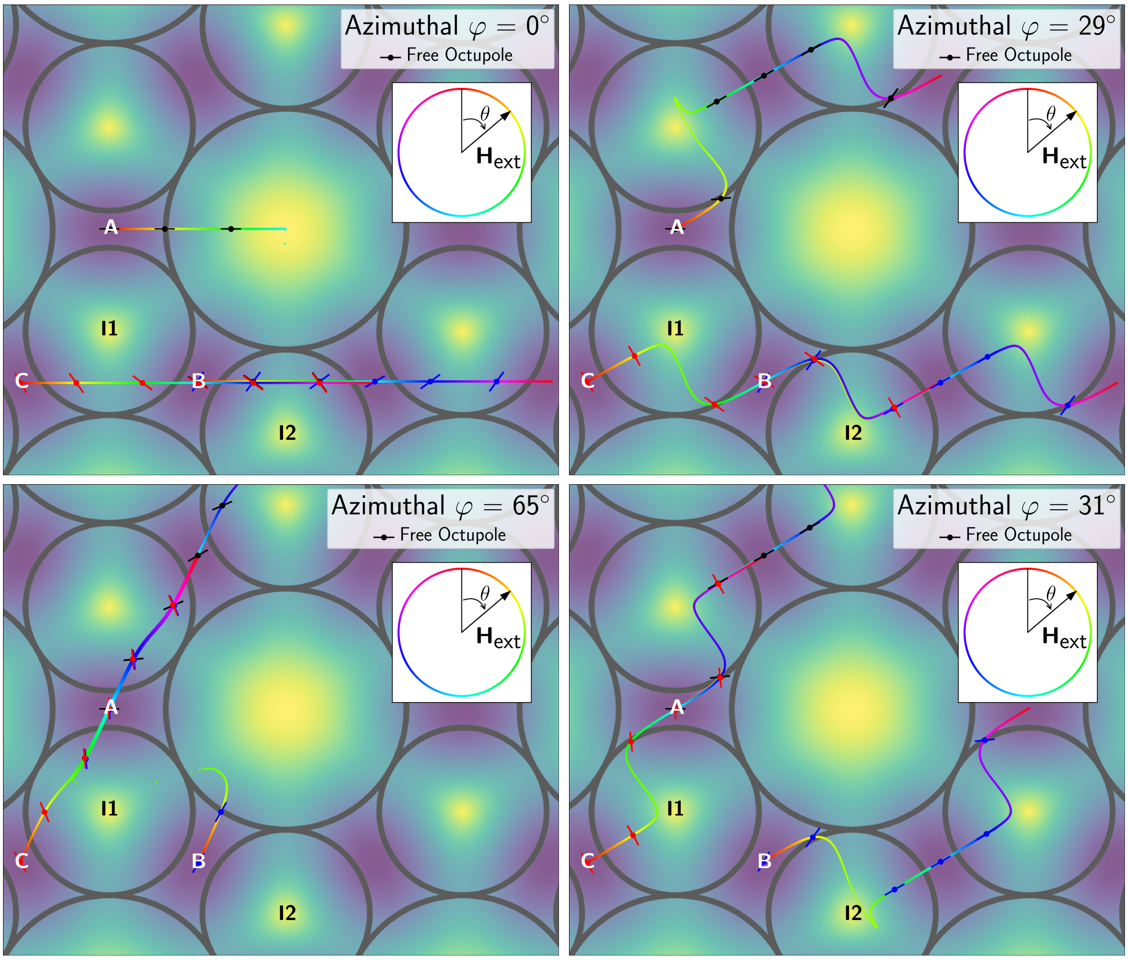

Figure 3.6: Paths of octupoles for different azimuthal angles in polar orbits, starting in one of the basins A (black), B (blue) or C (red). Depending on φ one octupole is on an unstable track and hops irreversibly to on of the stable positions (A in the top, B in the bottom). Along directions of high symmetry e.g. $\varphi = 0°$ or $60°$ the paths are straight and get deformed the further φ differs from these directions (top left, bottom left compared to right). A transition in transport direction and unstable basin occurs at $\varphi = 30°$. Top row is transported along $\boldsymbol{a}_1$, bottom row along $\boldsymbol{a}_2$. The paths are coloured according to the external field phase shown in the insets. The orientations are given at equally distanced times by the rotation of the octupole symbols.

seeking particle, behave differently, which can be seen in the top right of figure 3.7. Closer to the equator the octupoles and the saddle points behave similar again, though the shape of their paths differs quite strongly. Still, the non-trivial behaviour predicted in section 2.1 for a saddle point is verified by the saddle point data as well as by the octupole paths.

These data sets show that except for a small range of precession angles $\theta \approx 60°$,

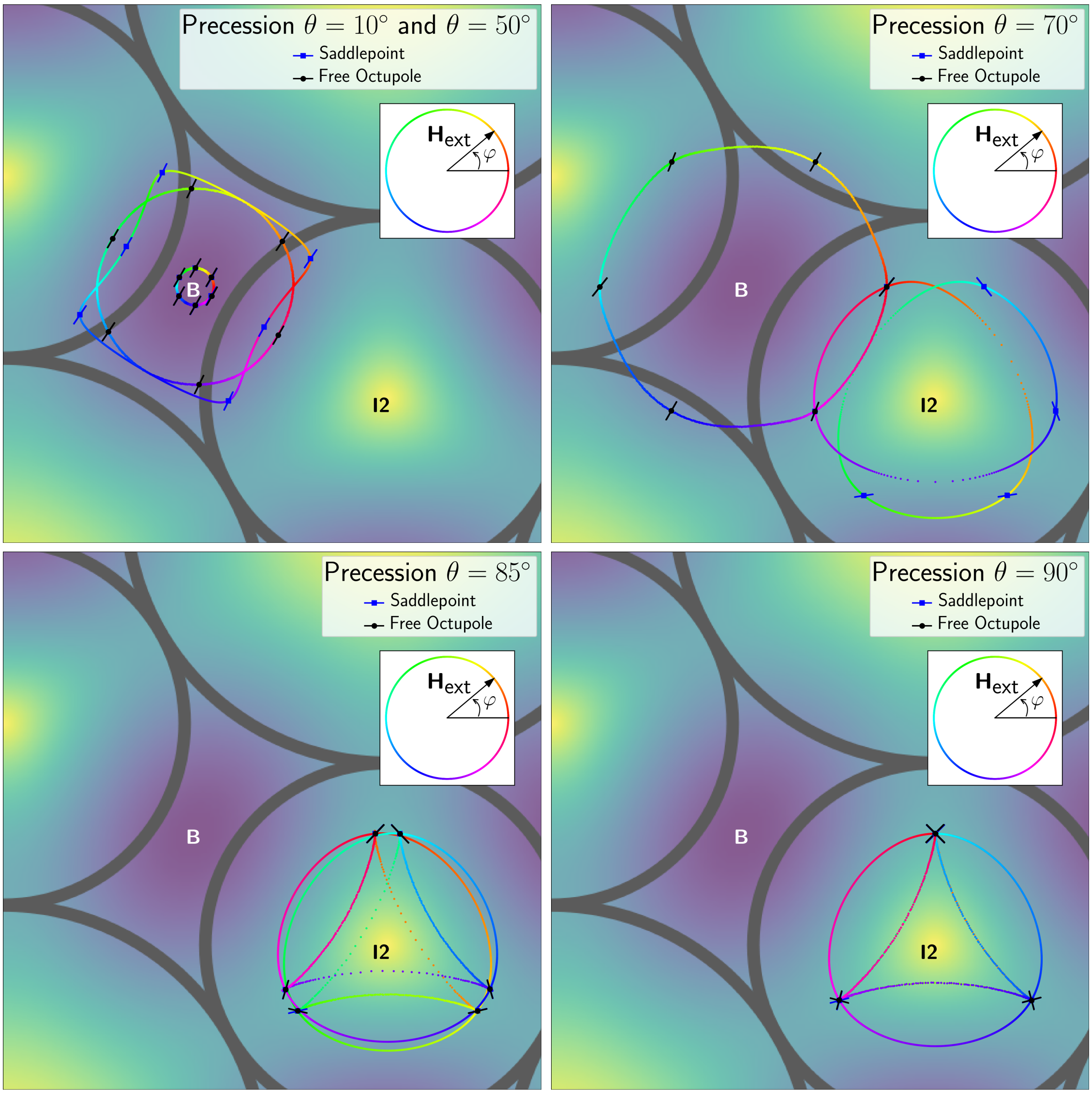

Figure 3.7: Comparison of free octupole paths with saddle point positions. No difference in position or orientation is visible for precession close to the poles (top left, inner paths). The form of the paths deviate for larger values of θ with six intersections at special field directions and comparable orientations (top left, outer paths). The saddle point transition occurs earlier than the octupole transition, giving raise to a region where both behave topologically different (top right) and only intersect twice. Closer to the equator the topology of the paths is the same again, the form differs with six intersections at special field directions (bottom row). The paths are coloured according to the external field phase as indicated in the insets. The orientation is indicated at equally distanced phases of the external field ($n\pi/3$ with $n \in [0, 5]$), in the top left these times are shifted by a phase of $\pi/6$ for better clarity.

free octupoles behave like saddle-point seeking particles in a topological sense. In both limits, close to the poles and close to the equator, the same paths topology is found. Therefore, free octupoles are protected by the same underlying topology as the particles seeking maxima and minima investigated in Löhr *et al.* (2016) and Rossi *et al.* (2017). This topological protection makes their movement robust against small perturbations like a random Brownian force.

3.1.4 Pattern symmetries

Apart from the described C_6 pattern, with proper rotational symmetry, a smooth transition towards a S_6 symmetry is possible by introducing a phase factor ϕ as shown in section 2.6. The S_6 symmetry has improper rotational symmetry, therefore a rotation of $\pi/3$ must be combined with a reflection along some given axes to retrieve a pattern symmetry. For each pattern three points of at least three fold rotational symmetry, C_3, exist as described in Löhr *et al.* (2017). For special phases ϕ, one of these can acquire C_6 or S_6 symmetry.

The potentials and the simulation results for free octupoles placed on these potentials are presented in this section. At other symmetries new loop types arise. These path loops give further insight and understanding into the topological transition from basin loops to double-triangle loops. Only precessing $\mathcal{C}$-loops are used to drive the octupoles in this section.

Potentials

In figure 3.8 the free octupole potentials for different patterns are shown for an external field pointing exactly north. By varying ϕ, the symmetry changes from C_6 for $\phi = 0$ to S_6 at $\phi = \pi/6$. The S_6 pattern can e.g. be build macroscopically with equal sized magnets and empty spots as indicated by the circles in figure 3.8. Values of ϕ greater than $\pi/6$ transform the pattern back into a C_6 pattern, now centred around one of the other symmetry points (blue and red triangles in figure 3.8).

In the case of a C_6 symmetry, the point of highest symmetry is centred in the inaccesible region I0. The other two symmetry points indicate the position of the interstitial I1 and I2. For symmetries varying from C_6 the two interstitials are not equal any more. One becomes the major interstitial surrounded by the basins and the other the minor one, which is connected to I0 with a potential ridge. For an

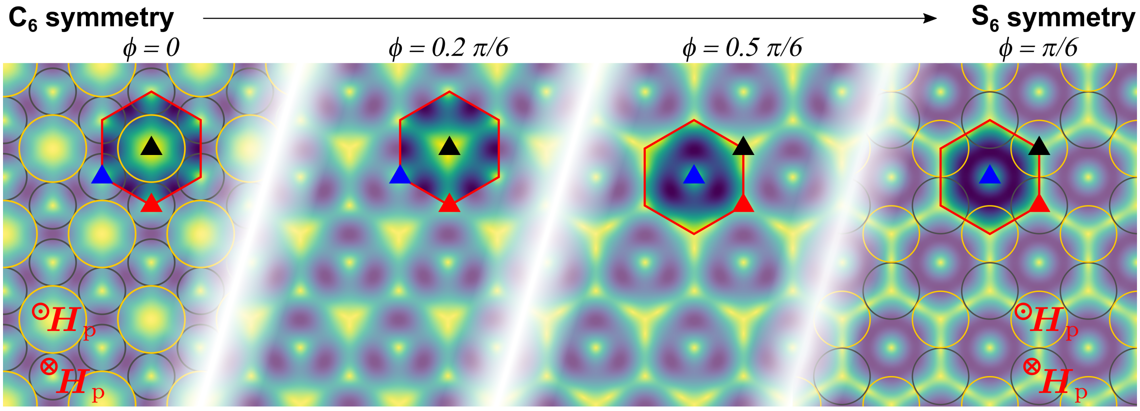

Figure 3.8: Potential landscape for different symmetries of the pattern. From left to right: the symmetry's phase ϕ changes the C_6 symmetric pattern into a S_6 pattern. For the extreme cases the magnets of a macroscopic pattern are indicated by yellow (grey) circles, that are magnetized up (down). Each lattice has three points per unit cell showing a C_3 symmetry. These are indicated by a red, a blue, and a black triangle. One of these can show a proper (C_6) or improper (S_6) 6 fold symmetry for special values of ϕ. For $\phi = 0$ the highest symmetry is at the black point above I0, for $\phi = \pi/6$ around the blue point at I1. In between the major (blue) and minor (red) interstitials are no longer equivalent. In each potential, one unit cell is depicted in red. The unit cells are located around the lattice points of highest symmetry in the extreme cases. Note that the symmetry relates to the underlying magnetic pattern, not the resulting potential, that always shows at least S_6 symmetry.

S_6 symmetric pattern the minor interstitial and the I0 region are now equivalent, leaving one clear interstitial in the center of a big blue basin.

The symmetry of the potential landscape always shows at least a S_6 symmetry during this transformation. This originates from the invariance for the free octupole potential under a transformation exchanging the direction of magnetization in the individual regions. The octupole's orientation merely changes by $\pi/2$, the positions are kept unchanged and therefore the potential landscape is unchanged.

Paths topology and orientations

The simulation results show further loop types of free octupoles, that are topologically distinct from those presented in section 3.1.1. The new loop types are shown in figure 3.9 and an overview of the full phase-space is given in figure 3.10.

Starting with a precessing field close to the poles we get trivial basin loops, the octupole's paths in $\mathcal{A}$, in all symmetries. However, the basin in the **pure $\mathbf{S_6}$ case** is now split into six basins, giving the possibility of six independently stable octupoles.

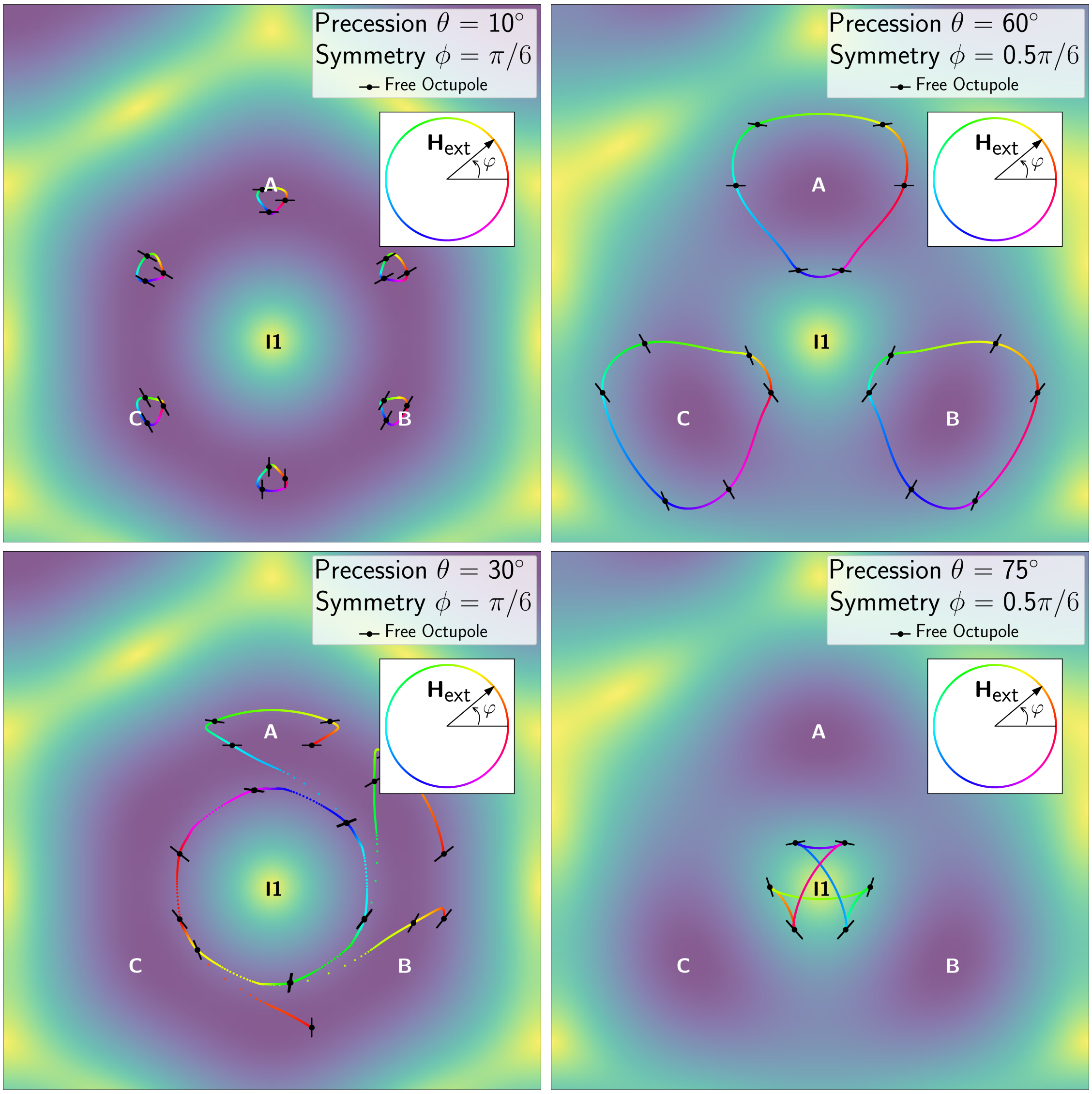

Figure 3.9: Simulated paths of free octupoles placed on a pattern with a symmetry other than a C_6 symmetry. **Left side** of the figure shows a full S_6 symmetry around I1. For small precession angles six stable positions are possible, leading to six **basin loops**. For larger angles these collapse into one big circle, the **attractor loop** around I1 with a orientational phase rotation of π during one field $\mathcal{C}$-loop. The attractor loop gets fed by six **feeder loops**, that are irreversibly emptied during the first field cycle. **Right side** of this figure shows an intermediate symmetry ($\phi = 0.5\pi/6$). Deformed **basin loops** are present at small values of θ. Driving fields with a larger precession angle lead to a path around the remaining interstitial that winds around the center once per external field loop ($W = 1$) in the same direction as the driving field. Three handles connect the segments of this **handle loop**. Close to the equator of $\mathcal{C}$ the non-trivial double-triangle loop shown in figure 3.3 with winding number $W = -2$ is retrieved again. A smooth transition shifts the inner branches of the loop with $W = 1$ to the other side of the interstitial point leading to $W = -2$. The paths are coloured according to the external field phase as indicated in the insets. The orientation is indicated at equally distanced phases of the driving field. The driving is in a positive sense.

In Löhr *et al.* (2017) a monkey saddle of U is described for this particular symmetry. Combining the three-fold symmetry of the monkey saddle with the two fold symmetry of the octupoles explains the existence of six stable positions.

Furthermore, the S_6 case shows a different winding behaviour around the interstitials. As shown in figure 3.9 after a topological transition the octupoles move around the interstitial in one big circle just once per external field $\mathcal{C}$-loop with winding number $W = 1$. The speed of the octupole on this **attractor loop** is not uniform, but can be split into six slow segments inherited from the basin loops and six fast connection parts. When starting the driving field, the octupoles still start in one of the six basins. These basins get emptied during the first field cycle leading to **feeder loops**, that are irreversibly emptied once the particle reaches the attractor loop.

As only one interstitial remains, only one independent octupole position remains for $\mathcal{C}$-loops approaching the equator. Closer to the equator of $\mathcal{C}$, the attractor loop's size decreases leaving just one stable point in the center for an arbitrary external field on the equator, making this remaining interstitial accessible for octupoles.

The orientations of the newly inserted basin positions are rotated by $\pi/6$ compared to the neighbouring ones. On the attractor loop, the octupole adapts to each basin orientation Φ_i along the path, again resulting in a rotation of $\Delta\Phi = \pi$ for a $\mathcal{C}$-loop cycle. Even in the case of a precession along the equator of $\mathcal{C}$ this orientation behaviour remains, such that the free octupole, that sits in one position, rotates with half the angular velocity of the external field.

Other symmetries show a topologically equivalent behaviour to the C_6 case for precession angles close to the poles. The occurring basin loops are slightly deformed, respecting the three fold symmetry that remains for all values of $\phi \neq n \times \pi/6$ with $n \in \mathbb{Z}_0$. Nevertheless, the transition towards the non-trivial double-triangle loops shown previously in figure 3.3 no longer is the same. From the basin loops (winding number $W = 0$) a transition towards a **handle loop** leading the free octupoles once around the interstitials in the direction of the driving field occurs. The segments of the triangle of this transition state are connected with "handles" that get smaller for symmetries closer to a S_6 pattern. The winding number around the interstitial of a handle loop is $W = 1$, while the rotation for all paths around an interstitial remains to be π. Larger values of θ deform this paths in a way, that the inner path segments move towards the center of the triangle. At this point the transition towards the double-triangle loop around the interstitials occurs, with a winding number of two ($W = -2$).

The range of precession angles θ, in which handle loops occur, grows with larger deviations from a fully C_6 symmetric pattern as shown in the phase diagram 3.10.

Besides the major interstitial, a minor interstitial exists, vanishing only in the pure S_6 case. If the deviation of the C_6 pattern is still small, for precessing fields close to the equator the double-triangle and triangle loops around the minor interstitial get stable again. In between, the area inside of a loop that remains as an intersection of all paths' segments, is too small to cover the larger extension of the minor interstitial. Therefore, a second stable octupole exists only close to the equator for symmetries close to a C_6 symmetry.

The change in paths topology and stable positions throughout different symmetry values of ϕ and different precession angles θ are summed up in the phase diagram 3.10. The change of loop size is encoded in the brightness values of the individual panels. Brighter values encode a smaller remaining area inside the loop. In the extreme case the colour white encodes the single stable point.

It can nicely be seen, that a transition from one symmetry type towards the other occurs. The attractor loop in the S_6 case arises from the handle loop by shifting the inner segments further out, growing in size and thereby closing the handles. Whereas the double-triangle loops originate from handle loops whose intersection area decreases until it vanishes completely, when the segments cross the interstitial point, they open up to the double-triangle loops with winding number $W = -2$.

Looking at all symmetries gives more insight into the nature of the topological transitions taking place in a single symmetry, especially for the pure symmetries S_6 or C_6, in which some phases are missing.

3.2 Braiding with free octupoles

After studying the behaviour of a single free octupole subjected to an external, driving field and a pattern field of given symmetry, the question arises, whether non-trivial movements can be created with a pair or a bunch of free octupoles.

The phase diagram 3.10 gives insight to the number of stable positions throughout the phase space. During experiments, the pattern symmetry is fixed at ϕ, leaving just the external field as a control parameter. Complex movements can certainly be performed on all patterns, transporting octupoles across a magnetic lattice in a topologically protected way. In Löhr *et al.* (2017) individual transport was studied

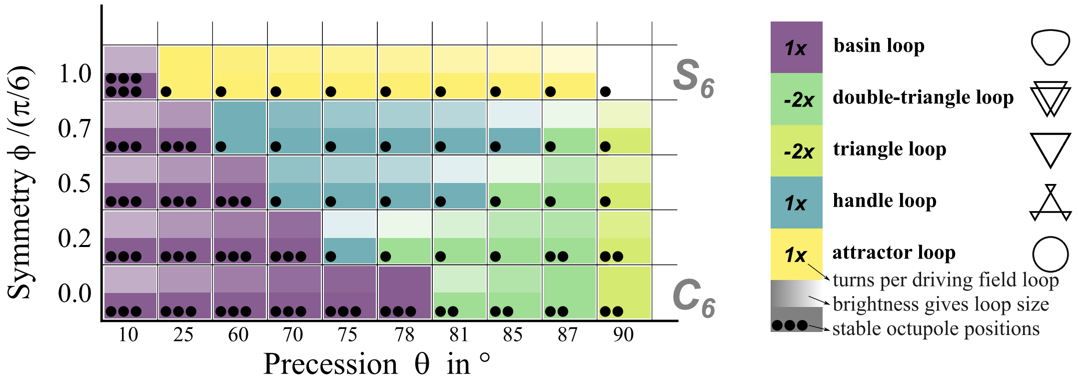

Figure 3.10: Phase diagram of paths topology and number of stable positions for free octupoles, subjected to precessing $\mathcal{C}$-loops (precession angle θ) and placed on magnetic pattern of different symmetry. The symmetry parameter ϕ is zero for a C_6 pattern and one for a S_6 pattern. The colours of one panel indicate different loop types, the brightness of the upper half of each panel indicates the size of the area included inside the loop. Darker colours correspond to larger areas. The purple panels correspond to the trivial **basin loops** analogue to those in figure 3.2. The green colours correspond to the non-trivial **double-triangle loop** and the **triangle loop**, winding twice ($W = -2$) around either interstitial I1 or I2 in figure 3.3. Blue loops are **handle loops**, winding once ($W = 1$) around the interstitial (compare bottom right of figure 3.9). They form a transition state between the basin loop and the double-triangle loop. Yellow decodes the circular attractor loop around the interstitial (compare bottom left of figure 3.9), only found for a S_6 symmetric pattern with a winding number of $W = 1$. The dots give the amount of stable positions per unit cell. Each tile represents one combination of θ and ϕ. Mind, that neither axes is split evenly, but the θ axis is split according to new transitions happening in one of the five symmetry cases studied.

---

extensively using paramagnetic or diamagnetic spheres on a microscopic patterns. All systems studied so far had in common, that only one minimum per unit cell can be used to manipulate the probe particles. This results from the fact that during one $\mathcal{C}$-loop, covering all major regions of $\mathcal{C}$, only one stable position remains. If the pattern symmetry allows for a second minimum, the second minimum is irreversibly emptied at some time during the driving $\mathcal{C}$-loop. Here, one case is of special interest: the previously studied C_6 symmetric pattern. As discussed in section 3.1.2 two octupoles can possibly be transported into individual directions.

In the following sections, this movement in individual directions will be discussed. First, control $\mathcal{C}$-loops, that allow the exchange of two octupoles will be developed. Second, the exchange $\mathcal{C}$-loops will be combined to allow more complex movements with more than two octupoles.

3.2.1 Exchange loop

Without loss of generality we start with two octupoles a and b, sitting in the A and B basin of one unit cell respectively. The aim is to end with these two octupoles being exchanged in the same unit cell, i.e. in the final situation octupole a sits in basin B and octupole b in basin A with no net displacement. Firstly, the necessary $\mathcal{C}$-loops are developed. Secondly, the resulting path data from the simulations is presented.

Such $\mathcal{C}$-loops will certainly include external field $\mathcal{C}$-loop segments in both, the north (south) and tropics region of $\mathcal{C}$. Furthermore, especially the relative positions of the different octupoles is important. Reminding ourselves of the position of octupoles relative to the external field phase in figures 3.2 and 3.3 gives the necessary information to create exchange $\mathcal{C}$-loops. Furthermore, section 3.1.2 showed, that a change of θ will transport the octupoles radially according to the current value of φ. This will be used to connect the $\mathcal{C}$-loop segments of different precession angles and will no longer be discussed separately.

As both free octupoles must not be in the same basin or interstitial at any time, we need to make use of the third, empty basin for a successful exchange. The exchange will then happen such that one octupole, e.g. b, goes via I1 into basin C. Then the other octupole (a) can cross directly into the final basin B before the octupole b can reach its final basin A. From figure 3.2 we conclude, that while octupole b does the sidestepping move into basin C, a enters the interstitial I2. The paths have to be designed such that a goes back into basin A, when b leaves I1 into basin C. There are two waiting positions or turning points, where b could enter basin C. In figure 3.3 (upper right) these are coloured red and yellow according to the external field phase. Comparing this to the path around I2 shows that octupole a, leaving I2 at the red segment, ends in a basin B of a neighbouring unit cell. However, leaving the interstitial on the yellow turning point, leads the particle a back into the basin A. Hence, we need to leave the interstitials at the second, yellow, position in order to keep octupole a, which is currently located on I2, in the original unit cell.

Combining $\mathcal{C}$-loop segments in this way gives a toolbox to construct the whole loop, the path in $\mathcal{A}$, as desired. We are free to choose fields from one (the upper) or from both hemisphere. For both choices an example loop is shown in figure 3.11. In the upper half the external field always switches between both hemispheres, whereas the lower part only uses fields in the northern hemisphere, but allows for a backwards running field, making the total path shorter. Although both ways exchange the

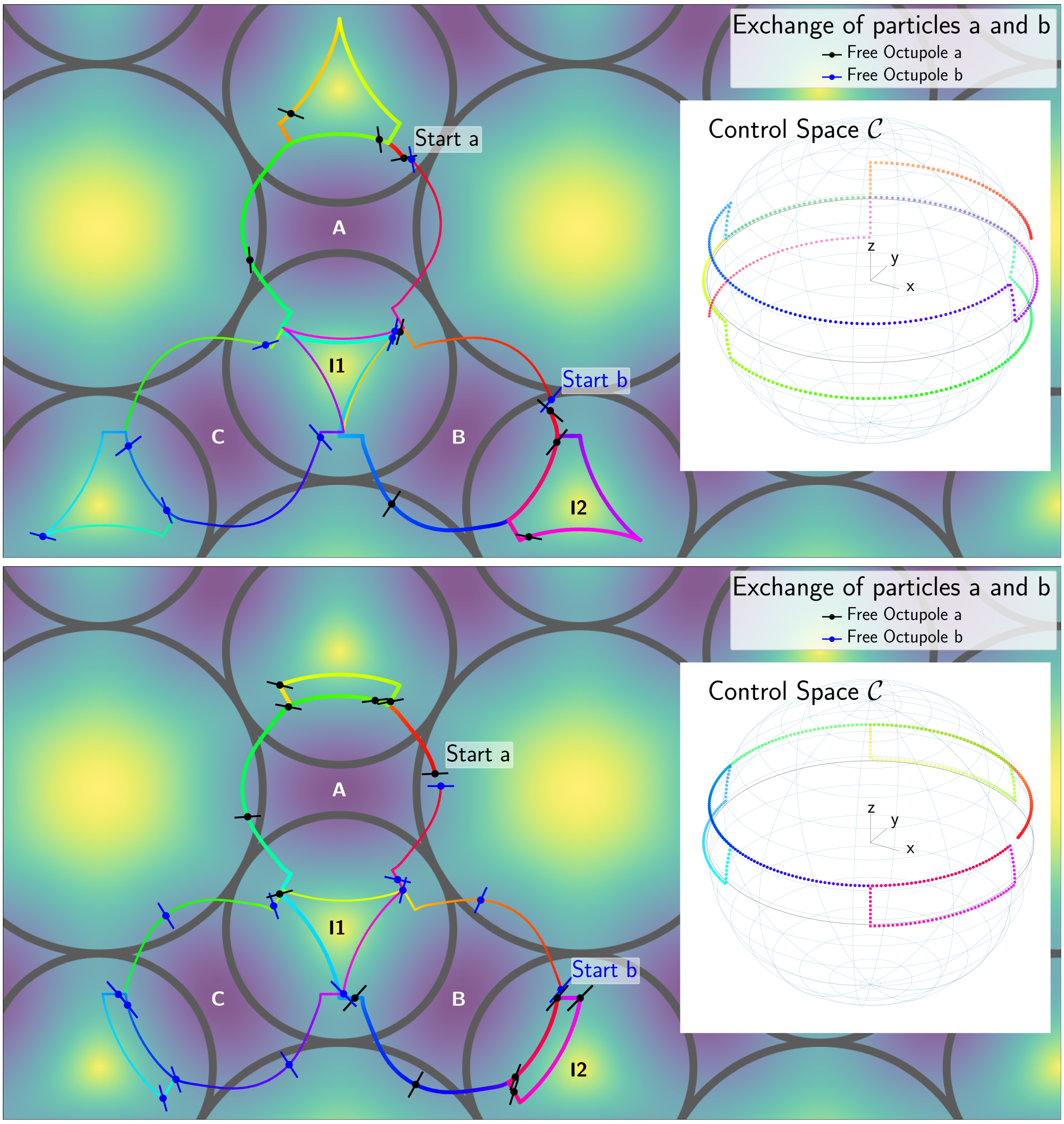

Figure 3.11: Two $\mathcal{C}$-loops exchanging the free octupoles initially located in the north-west of basins A and B. The paths of the loops are coloured corresponding to the phase of the external field $\mathcal{C}$-loop shown in the inset. In both cases, the octupole b (blue, starting in B) sidesteps into basin C such that octupole a (black, starting in A) can cross via I1 into basin B. In the **upper case**, fields in both hemispheres are used and the octupoles end up with an effective orientation of $\pi/2$. Bringing the octupoles back to their original basins is therefore only possible with an inverse field (starting in the south). In the **bottom case**, only fields in one hemisphere (north) are used, their final orientation is the same as the initial $\Phi(T) = \Phi(0)$. Bringing the octupoles back to their starting point is possible by repeating the $\mathcal{C}$-loop. After a second exchange, octupole b effectively surrounded octupole a clockwise, making this exchange non-trivial. The octupoles' orientation is indicated at equally distanced times. To gain a better visibility, the paths of the octupoles b are plotted slightly shifted and the paths of octupoles a are drawn slightly thicker .

octupoles a and b, one difference remains. The second path is a closed $\mathcal{C}$-loop, the first $\mathcal{C}$-loop ends in a point exactly opposite to the starting point of the driving field. This explains the different orientations of the octupoles after the exchange.

If we now bring the free octupoles back into their original basin by exchanging them a second time, we can effectively wind one octupole around the other. By applying the same $\mathcal{C}$-loop in the bottom case of figure 3.11 or a $\mathcal{C}$-loop with an inverse field in the top case leads to the same exchange movement as before. The bottom octupole (now a) sidesteps into basin C to let octupole b cross back into basin B. This effectively is a clockwise winding of octupole b around octupole a.

The phase of the orientation, accumulated by one octupole during such $\mathcal{C}$-loops, differs with different $\mathcal{C}$-loop types. In the upper case, octupole a rotates by $\Delta\Phi = -{}^{23}\!/_{18}\,\pi$ and octupole b by $\Delta\Phi = -13/18\,\pi$. Bringing them back to their origin therefore leads to an effective rotation of $\Delta\Phi = -2\pi$. In the bottom case of figure 3.11, octupole a only rotates by ${}^{5}\!/_{18}\,\pi$ and b by ${}^{13}\!/_{18}\,\pi$, leading to an total reorientation of $\Delta\Phi = +\pi$ after a full winding loop.

3.2.2 Braiding loop

After constructing and demonstrating the exchange loop of two octupoles, we want to shuffle more than two octupoles in the action space. In this section the braiding $\mathcal{C}$-loop is motivated and constructed leading to a braiding group of free octupoles on a C_6 pattern.

As action space $\mathcal{A}$ is two dimensional, the winding of one octupole around the other is a topologically non-trivial movement as introduced in section 2.2. Therefore, braiding with free octupoles is possible and we can introduce a braiding group for the octupoles. If we take only two octupoles and attach a virtual or real string on top of the free octupoles, fixed at some point above the lattice, we have a macroscopic configuration of the $\mathcal{B}_2$ group with the operators σ_1, σ_1^{-1} and $\mathbb{1}$.

Adding a third free octupole a' without loss of generality to another basin A introduces more possibilities. Octupole b can either wind around the previous octupole a by crossing over interstitial I1, or around the newly added octupole a' by crossing I2. This winding can be both either clockwise or counterclockwise. As the octupoles a and a' can not be exchanged, it is not a full $\mathcal{B}_3$ braiding group. We can create a subgroup $\mathcal{B}_3^{\oplus}$ that only takes elements of $\mathcal{B}_3$ where the strings end in the same positions as they start. The generators therefore are $\hat{b}_1 = \sigma_1\sigma_1$ and $\hat{b}_2 = \sigma_2\sigma_2$ where

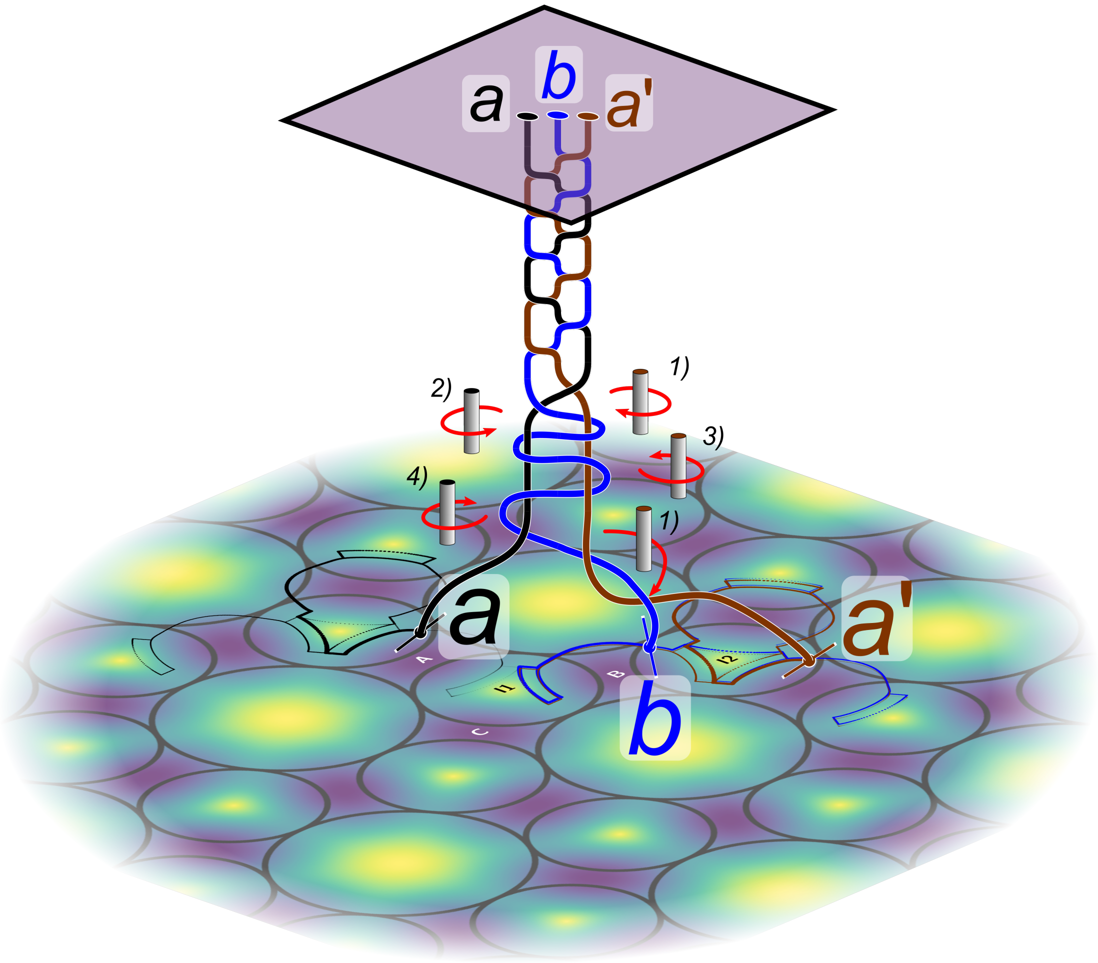

Figure 3.12: Three octupoles, marked black (a), blue (b) and brown (a') are exchanged on a C_6 pattern. Octupole b is winding clockwise around a'. The pattern is indicated by the potential landscape. Their preceding paths are indicated by coloured trajectories on the potential. The more recent part of the trajectory is thicker, whilst the parts further back in time are getting thinner until they vanish. Virtual strings connected to a fixed plane above the pattern are attached to the octupoles. The evolving braid shows the past exchange behaviour. b was winding around a and a' in the following self repeating sequence: **1)** clockwise around a', **2)** counter clockwise around a, **3)** counter clockwise around a', **4)** clockwise around a. This sequence effectively leads to a braiding of the three strings, as indicated close to the fixed plane. The transformation from the winding of b around both of the other strings towards the common braid is smooth. The movement of octupoles a and a' is always parallel as the octupoles a and a' cannot change place. Winding of those two octupoles is not possible and it depends on octupole b, which of the octupoles a or a' is involved in the winding procedure. The black string is always in front of the brown one after a smooth transition towards a braid.

octupole b is either winding via I1 clockwise around a or via I2 clockwise around a' respectively. The generators $\hat{b}_1$ and $\hat{b}_2$, together with the inverse, counter clockwise winding generators $\hat{b}_1^{-1}$, $\hat{b}_2^{-1}$, and the unity generator $\mathbb{1}$ form a sub group of $\mathcal{B}_3$. The subgroup still forms a non-abelian group as $\hat{b}_1\hat{b}_2 \neq \hat{b}_2\hat{b}_1$.

Most commonly known as braiding is the braiding with three strings of e.g. hair to a braid. Although this technique mostly involves exchanging all three strings at some point in time, it is an element of $\mathcal{B}_3^{\oplus}$. The same topology can be archived by the following combination of winding the middle strand around one of the others:

$$\hat{b}_{\text{braid}} = \hat{b}_1\,\hat{b}_2^{-1}\,\hat{b}_1^{-1}\,\hat{b}_2 \tag{3.1}$$

The octupole b is first winding clockwise around a', then counter clockwise around a, counter clockwise around a' and clockwise around a. This is best seen with real strings and trying it out on your own by just pulling the strings, especially the middle string, after the winding procedure is finished. It is also shown in figure 3.12 and can be understood by looking deeper into the process. The common braid is created by taking the right above its neighbour into the center, then the left string above the new center sting and so on. In the end string a is always placed on top of string b, b always on top of a', and a' always on top of a. The two strands a and a' effectively never wind around each other and can be brought in a parallel configuration in which b winds around both which is exactly the case we can simulate with our octupoles. The braiding operation is sketched in figure 3.12.

Taking other generating $\mathcal{C}$-loops will create other types of braids. Unless a generator $\hat{b}_1$ or $\hat{b}_2$ is followed by its inverse, the braid saves the information about the generating $\mathcal{C}$-loop, as an unwinding is only possible by applying the appropriate inverse $\mathcal{C}$-loop.

Depending on the $\mathcal{C}$-loops creating the actual exchange, a different rotational phase of the octupoles may be accumulated.

3.3 Locked octupoles

In section 2.5 a second type of octupole was introduced. Until now we only studied the behaviour of free octupoles. In this section, simulations on the trajectories of locked octupoles will be studied. The octupoles are locked to the projection of the driving field $\boldsymbol{H}_{\text{ext}}$ onto the action space, hence the azimuthal angle φ of the driving field. The relative angle between the octupoles orientation and the projection of the external field is therefore fixed. According to the choice made in section 2.5, the orientation of the octupole is

$$\Phi(t) = \varphi(t) + \gamma + \pi/2. \tag{3.2}$$

The change in orientation is therefore locked to the external field behaviour. Only the position can adapt to find an energetically favourable position. A free octupole on the other hand has its orientation as an extra degree of freedom. The minima that can be found by a free octupole are therefore at least as energetically favourable as those found by a locked octupole. The free octupoles' minima are mostly energetically way more favourable and the locked octupoles want to be as close to those minima as possible. But their rotational locking doesn't allow to follow these minima for an infinite period of time. In a first approximation, for orientations Φ_{locked} close to those of a free octupole at the same position, the minimum is still attractive. After a while however, the difference in orientations is too large and attraction can no longer be guaranteed. The octupoles jump towards the next stable position, mostly involving a ratchet. This is the driving mechanism for the path loops shown in the following section.

The simulations are done using the forces and scripts described in chapter A. All data shown here is calculated for an octupole with size $r = 0.06a$, which is in agreement to the size of the octupoles used in the experiments in chapter 4. The random force was set to zero to archive comparable results. The influence of the random force was stronger than in the case of free octupoles according to the argument, that the potential minima can never be deeper than in the free octupole's case. Small deviations from the perfect paramagnet-diamagnet ratio were found to have only a small influence. However, larger deviations led to the same class of loops in $\mathcal{A}$, found for single paramagnetic or diamagnetic particles with slight deformations throughout the path.

The results presented in this section are those of a perfectly balanced locked octupole, δr and $\delta\chi$ introduced in chapter A are set to zero. The driving field $\mathcal{C}$-loop is chosen to be either a precessing $\mathcal{C}$-loop or a orbital $\mathcal{C}$-loop. Both types of driving the locked octupoles are presented in this section.

3.3.1 Path types for precessing fields

Analogous to the free octupoles, we start driving the locked octupoles with a precessing external field. The octupole's path loops, resulting from the simulations, are presented and discussed in this section. The overall behaviour can be described by slow segments close to stable positions of free octupoles that are connected by fast segments generated by ratchets. Different locking angles of the locked octupole lead to a different phase in a loop, that makes a certain basin stable. For each locked octupole, a certain but differing segment of the free octupole's path is stable. Based on these argument we can understand the simulated paths presented figures 3.13 and 3.14.

For small precession angles, the stable positions of the free octupoles are always very close to the center of the blue basins as shown in figure 3.2. Changing the octupoles orientation by rotating the external field forces the locked octupoles to jump to the next basin after $\varphi(t) = \pi/3$. A different locking angle only leads to a different starting basin in an external field $\mathcal{C}$-loop. This is a consequence from the proximity of the stable free octupole positions for different external field phases φ.

For larger precession angles, the stable positions of locked octupoles with different locking angle are no longer close to each other and no longer in the center of the basins. This can be explained by the larger basin loops exhibited by free octupoles. Depending on the locking angle, the stable positions of locked octupoles are therefore further out, at the edge of some basin. In a certain basin, these stable positions can now be either closer to the large, inaccessible region I0 or closer to one of the interstitials I1, I2. This proximity to either I0 or I1, I2 creates two types of paths, that are shown in figures 3.13 and 3.14. The first path type, the **flower**, encircles a large area including even large parts of the basin areas. The second type, the **star**, is characterized by rather sharp tips and a smaller included area.

The flower is created by locked octupoles, that have their stable positions close to some I0 region. All locked octupoles follow the free octupole path for some while, until it is energetically unfavourable. Due to their sense of rotation, the closest stable position belongs to a basin adjacent not to the same, but a neighbouring I0 region. This spans a very large path encircling up to a whole unit cell.

The star shape however is created by all other locked octupoles. Two different chiralities of those star paths exist as shown in figure 3.14. If the stable segment leads the locked octupoles back towards I0, the subsequent fast segment brings the

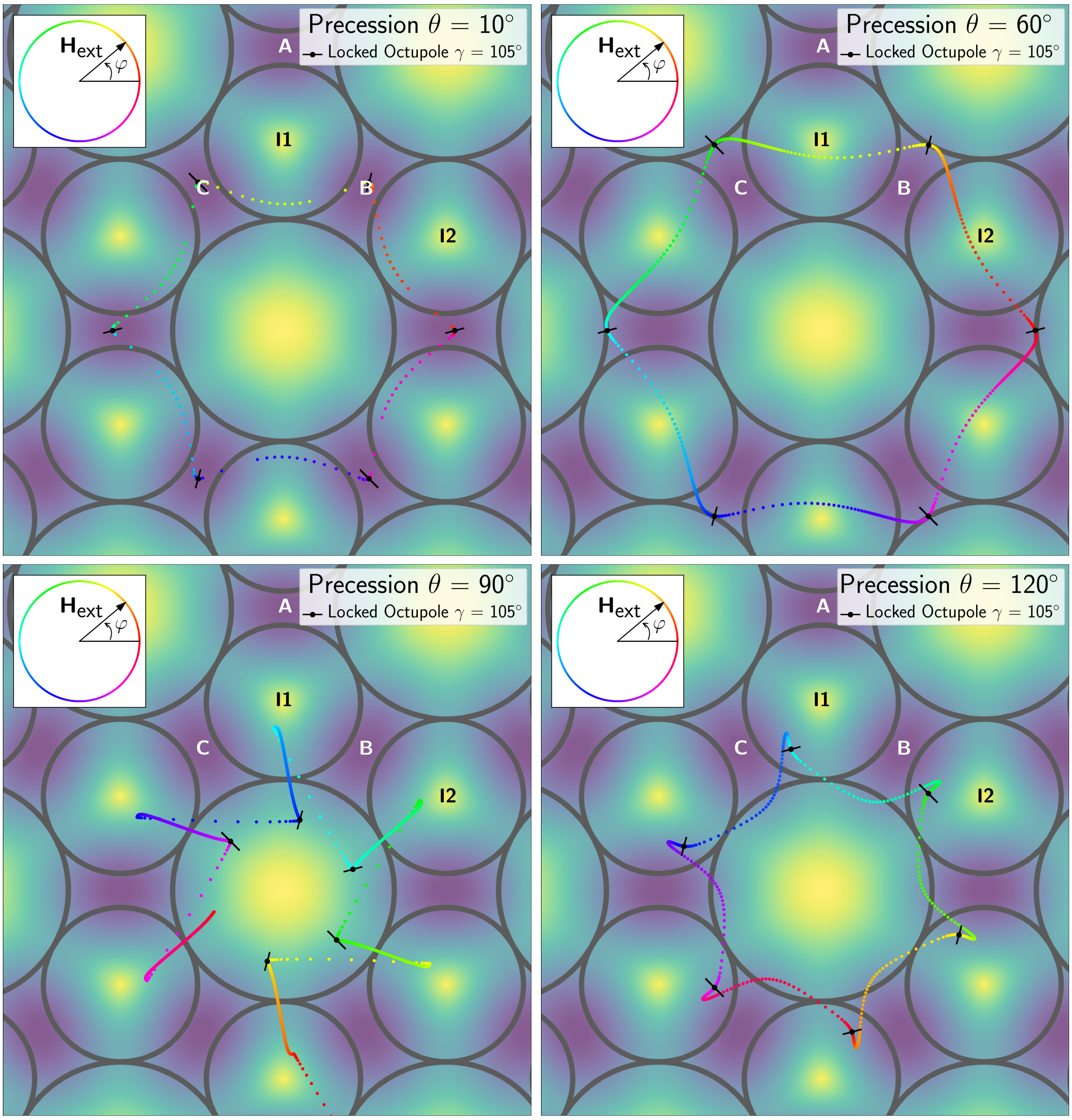

Figure 3.13: Paths of locked octupoles for different precession angles θ. All locked octupoles have a locking angle of $\gamma = 105°$. The driving is in a positive sense. The locked octupoles for $\theta = 10°$ (**upper left**) are sitting in the center of one of the basins A, B or C, where the free octupoles would remain, until they jump to an adjacent basin with better fitting orientation. Depending on the stable position of the free octupoles in the basin, the shape changes. For larger precession angles, the shape can either be more like a **flower** and include the basins (**upper right**) or more like a **star** (**lower right**). The path in the lower **left shows** a **Sisyphus phase**, with adiabatic moves from one of the interstitials towards the central I0 followed by clear ratchet jumps to an adjacent interstitial. In this case (lower left) the shape depends on the driving direction. The stable path segments can either be connected to a star (positive driving, shown here in the lower left) or a flower (negative driving, not shown here) including the basins. Inverting the driving direction does not change the path's shape in the top cases and the bottom right case. The paths are coloured according to the phase of the external field as indicated in the inset. The drawn data points from the simulations are evenly distanced in time.

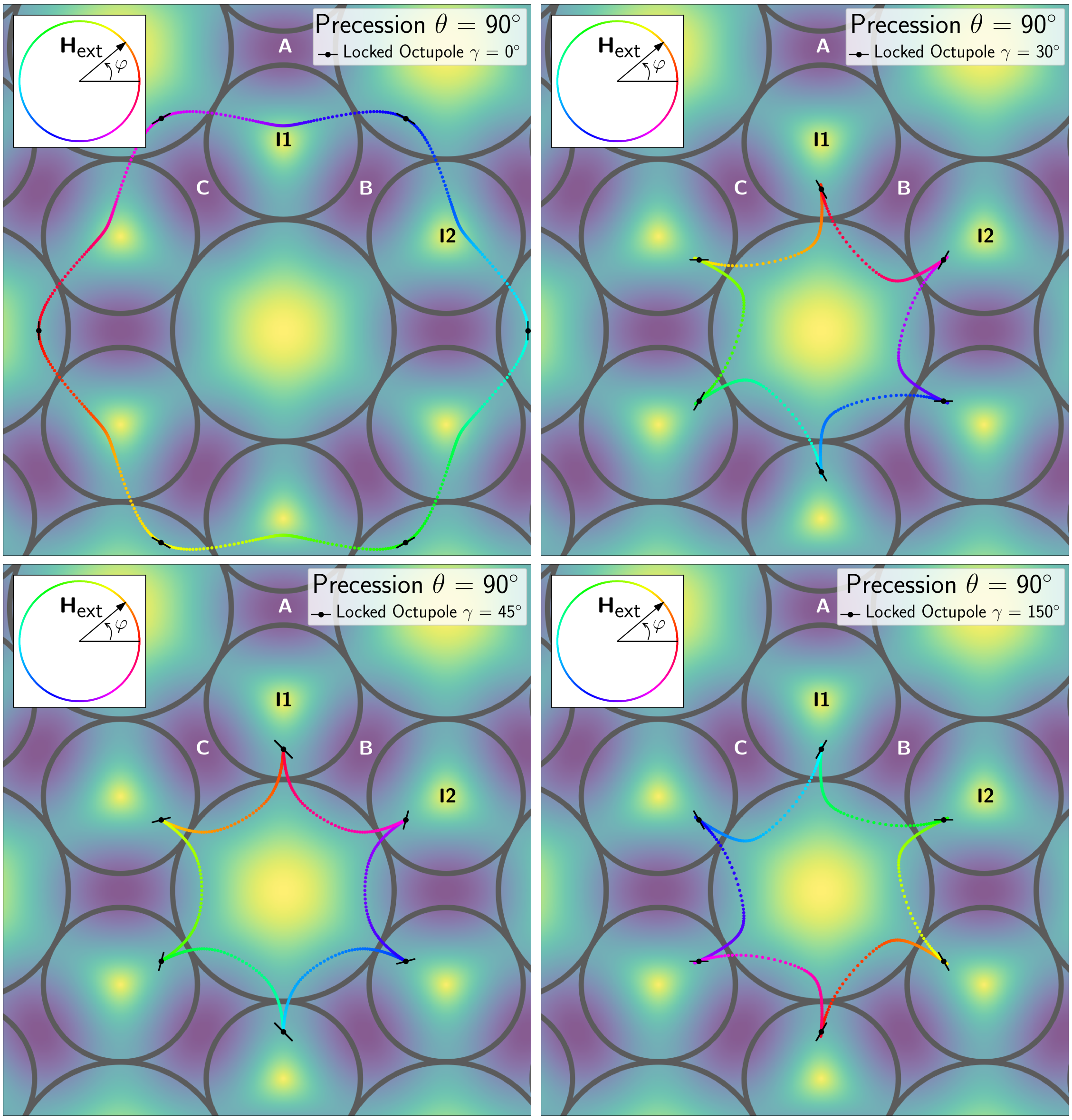

Figure 3.14: Paths of locked octupoles with different locking angles γ for a driving field along the equator. Two shape types, the **flower** (**upper left**) and the **star** (others) are found depending on the value of γ. For $\gamma = 45^\circ$ perfect agreement with the free octupole's position is found at certain times. The star path is symmetric in that case (**lower left**). For other cases, a slight asymmetry is found (right). The octupoles either approach a tip of the star with a ratchet (**upper right**) or leave the tip with a ratchet (**lower right**), leading to two different chiralities. Furthermore, the phase of a locked octupole in its path can differ as seen by the position of e.g. the red coloured segment of the paths. A phase shift of π in $\mathcal{A}$ relates octupoles with perpendicular orientations. The transition from a star to a flower happens via the driving direction dependent Sisyphus loop, shown in figure 3.13 in the lower left. The paths are coloured according to the phase of the external field as indicated in the inset.

octupoles to the next tip of the star. Otherwise the fast segments starts at the tip and brings the octupole to the next basin. This difference can be seen in figure 3.14 and leads to the two different chiralities of the shape of such paths.

Turning the direction of the driving field will mostly not change the chirality, as it is defined by the stable segments. Even the shape seems to agree in great detail in both driving directions. This indicates that the fast segments can not be a ratchet transition. However, the shape of the loop has no information on time and only with the time information that conclusion can be made. Only close to the transition between a star and a flower, the strong ratchet, connecting the adiabatic segments of the **Sisyphus phase**, is dependent on the driving direction. Changing the direction of the driving field switches between a star and a flower in the Sisyphus phase. In the bottom of figure 3.13, the Sisyphus phase is shown in the star shape.

Unlike in the case of free octupoles, for precessing fields close to the equator, no transition towards topologically different path types occurs. The stable path segments, and thereby the tips of the stars, are merely shifted towards the interstitials. Only for $\theta = 90°$, a star without any chirality exists for the special values of γ, matching the orientation of a free octupole at the tip of the triangular, non-trivial loop shown in figure 3.3.

A precession on the southern hemisphere leads to a change of the path's chirality. Analogue to pushing the tips of the star closer to the interstitial by approaching the equator, these stable positions are being pushed further into the next basin when crossing the equator. This is in agreement with the orbital transport loops shown in figure 3.6. When the stable segment was leading the octupole towards some I0 region before crossing the equator of $\mathcal{C}$, the stable segment now leads the octupole away from I0 and the path loop has the opposite chirality.

The shape retrieved from small precession angles (upper left in figure 3.13) is somehow an intermediate shape, transforming a star smoothly into a flower, as the basins are neither included nor excluded by the loop. Therefore a transition between a star and a flower either goes via these intermediate star/flower shapes or via driving direction dependent ratchets in the Sisyphus phase, shown in the bottom left of figure 3.13.

An overview over the occurring path types as well as their chiralities and orientations relative to the central I0 is shown in figure 3.15. Starting from indistinguishable shapes at low precession angles, a splitting into two types occurs. The symmetries of the system can nicely be observed. An external field $\boldsymbol{H}'_{\text{ext}}(t)$, that is the mirror image of $\boldsymbol{H}_{\text{ext}}(t)$ with respect to the x-y-plane leads to the same path's shape as $\boldsymbol{H}_{\text{ext}}$,

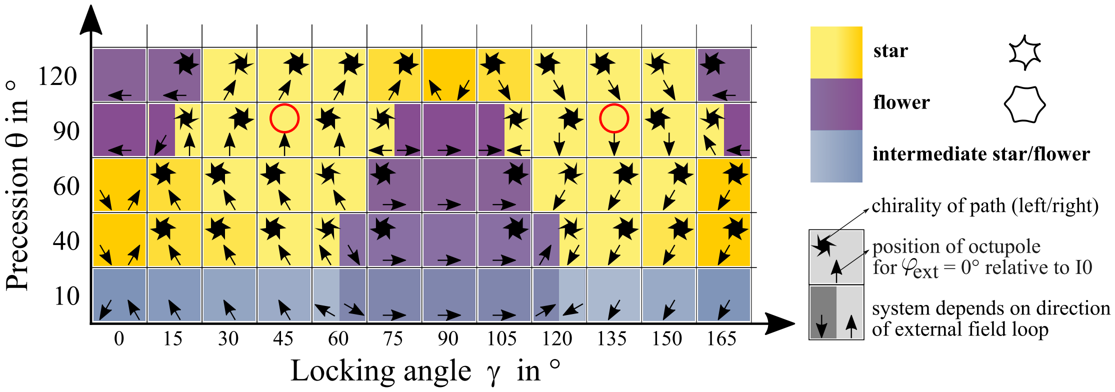

Figure 3.15: Phase diagram of the path types of locked octupoles shown in figures 3.13 and 3.14. The octupoles are locked to the external field with a locking angle of γ and driven by a precession $\mathcal{C}$-loop with precession angle θ. Each combination of θ and γ is represented by one panel in the diagram. The shape is colour coded, with purple indicating the flower and yellow indicating the star. Darker colours represent larger included areas of the paths. The chirality is indicated by the chiral star, depicted either in the left corner (stable segments lead the octupoles away from I0) or right corner respectively. The stars with narrow tips indicate a stronger chirality. The red circles mark the positions of vanishing chirality. The arrows in the bottom of each panel indicate the position of an octupole for $\varphi(t) = 0$ relative to the encircled I0 region. The direction of the arrow either depicts the basin, to which the stable segment belongs or (some cases in $\theta = 90°$ and $10°$) the closest interstitial. At some constellations of θ and γ, transitions occur and depending on the direction of the driving field, the outcome differs in shape and or direction, indicated by a split panel. Counter clockwise field $\mathcal{C}$-loops always correspond to the right side of the split panel.

if the locking angle of the octupole is shifted by $\pi/2$. When mirroring the driving field and rotating the locked octupole by $\pi/2$, only the loop's phase in the action space $\mathcal{A}$ differs by π, in agreement with the results of section 3.1.1. This symmetry accounts even at the equator. Taking the inverse of the driving field together with a orientation shift of $\Delta\Phi = \pi/2$ is therefore a symmetry of the system, leaving the path invariant.

The general behaviour of such locked octupole loops is a path running around one I0. This behaviour seems to be similar to the behaviour of paramagnets or diamagnets at a first glance. The huge difference is, that for para- and diamagnets I0 is accessible and their path loop can easily be contracted, such that they sit on the center of the central magnet for a driving field parallel (paramagnet) or anti parallel (diamagnet) to its magnetisation. The locked octupoles cannot go deep into the I0 region and always have a winding number of $W = 1$ around I0. Apart from that they can be distinguished by the amount of path in the basin region, which is inaccessible to both, para- and diamagnets. Finally, the flower is a behaviour not known for simple $\mathcal{C}$-loops for neither para- nor diamagnet.

3.3.2 Sorting with polar orbits

Apart from precessing fields, we further study the behaviour of locked octupoles driven by a polar orbiting field. The resulting trajectories from the simulations on systems with different locking angles and different driving $\mathcal{C}$-loops are presented in this section.

In section 3.1.2 the transport of free octupoles driven by a polar orbit of varying azimuthal angle φ is studied. Their orientation changes only slightly during the individual $\mathcal{C}$-loops, such that an octupole starting in B is always approximately oriented like an octupole, that remains in B. The locked octupoles do not only stay approximately oriented during a polar orbit, but stay perfectly oriented. Therefore, most of the trajectories and path shapes of free octupoles can, up to slight deformations, be reproduced with locked octupoles and will not be shown here. However, in the free octupole's system, discussed in section 3.1.2, octupoles starting in some basin, e.g. A, would relax irreversibly into another basin, when running into I0. A ratchet transition and a reorientation brought them into a new basin and back on a stable track. This is no longer possible with locked octupoles, as they must not change their orientation.

A locked octupole will end in a basin that is determined by its relative orientation γ and by the azimuthal angle φ of the driving $\mathcal{C}$-loop. Returning the $\mathcal{C}$-loop to the north pole forces the locked octupole into the best fitting basin, which depends on the octupoles locked orientation. The variation of the final basin with the orientation of the octupole can be used to effectively sort the locked octupoles by their locking angle γ. Starting at one basin, e.g. A, will lead different octupoles into different final basins. This is shown in figure 3.16. Apart from the basin, even the direction of motion varies between different locking angles, such that a sorting with one orbital $\mathcal{C}$-loop into six particle classes is possible. Although only a range of $\Delta\varphi = 110°$ is shown, a continuation of the diagram as well as different starting basins is possible for symmetry reasons.

The sorting itself happens via ratchets, that are quite robust if the external field direction is not aligned with some high symmetry direction of the pattern. This is analogue to the free octupole's case of section 3.1.2, where the transition of the

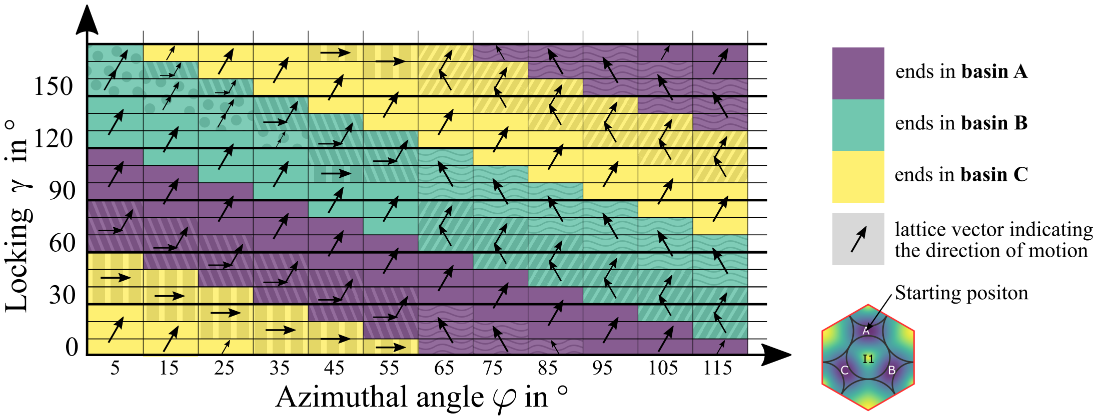

Figure 3.16: Phase diagram showing the final basins for locked octupoles subjected to a polar orbit. The octupoles all start in basin A. According to their locking angle γ and the driving azimuthal angle φ, the octupole ends in a different basin indicated by the colour of the panels. Furthermore, depending on the locking angle, the direction of the displacement varies as indicated by the arrows and the corresponding background pattern for better visibility. One arrow depicts one primitive lattice vector relating the centres of the unit cells before and after one $\mathcal{C}$-loop. The unit cells are centred around the interstitial I1. Each tiny panel corresponds to one locking angle and one azimuthal angle, both are varied in steps of 10°.

direction of the first ratchet emptying the unstable basin changes at multiples of 60° for fields aligned with the primitive lattice vectors. A comparison of the transition inbetween the individual loops is shown in figure 3.6.

As the direction of sorting and the end basin vary smoothly with the azimuthal angle, one can imagine that an arbitrary combination of orbital $\mathcal{C}$-loops can sort the locked octupoles placed in some fixed starting basins according to ones desires. By avoiding azimuthal angles that are multiples of $\pi/3$, the sorting is stable and reliable results can be expected.

4 Experiments

After studying the theoretical expectations for topologically protected transport of induced octupoles placed on a magnetic pattern in an external, driving field, this section covers the experimental realization of such systems.

The usage of high temperature superconductors (type-II-superconductors) in the construction of the octupoles leads to a pinning of magnetic flux quanta penetrating the superconducting phase. This effectively freezes the current state of the magnetic field into the superconductor and can be used for impressive effects like magnetic levitation (Brandt, 1990). The direction of the flux quanta is imposed by the external field direction inside the sample in the moment of the conductor-superconductor transition.

The pinning itself is quite strong compared to other torques in the system, leading to a composite particle, a locked octupole, that always aligns in the same orientation according to the magnetic field. As the external field is by choice strong compared to the pattern field, the alignment occurs with regard to the external field direction.

Therefore, an octupole consisting of two type-II-superconductors and two paramagnetic particles is supposed to behave like a locked octupole as described in section 2.5. A type-I-superconductor on the other hand can be used to create a free octupole, as the superconductors are perfect diamagnets due to the Meissner–Ochsenfeld effect. Unfortunately, the lab equipment of the Fischer group in Bayreuth does not allow for experiments at liquid helium temperatures. Hence we can't study free octupoles experimentally.

In this chapter, only experiments on composite particles using type-II-superconductors, therefore possibly locked octupoles, are presented.

Magnet	**Diameter**	**Height**	$\mu_0 M$
Pattern, center	3 mm	2 mm	1.19 T
Pattern, corners	2 mm	2 mm	1.35 T
External field	60 mm	10 mm	1.28 T

Table 4.1: Dimensions and magnetizations of the NdB-magnets used in the experimental setup. The integral of the magnetization over one unit cell vanishes.

4.1 Setup and implementation

4.1.1 Goniometer

The experiments were done on the macroscopic scale, using the goniometer already used for the experiments shown in Rossi *et al.* (2017). The setup can be seen in figure 4.1. The goniometer consists of a ring, a sled and the sample holder. The ring can rotate 360° around its support structure. The sled, mounted on the ring, can almost rotate full 360°, limited by the supporting axis of the ring. All supporting parts are build from non-magnetic materials (aluminium, brass, polymers) to avoid disturbances of the magnetic fields needed in the experiments.

A pair of large NdB-magnets is mounted on the sled, freely rotating along the ring and around the pattern. By rotating these magnets, the direction of the external, driving field $\boldsymbol{H}_{\mathrm{ext}}$ can be adjusted to induce transport of the probe particles. The magnetization of the magnet is given in table 4.1.

In the center of the goniometer, the magnetic pattern is located. It is built from cylindrical NdB-magnets with two different diameters. The magnetisation of the larger magnets points upwards. The orientation of the smaller magnets points downwards. The resulting pattern is shown on the left side in figure 3.1 and in the 3D representation in figure 4.2. The magnetizations are chosen such that the magnetic moment of one unit cell vanishes. The magnetizations are listed in table 4.1. The pattern is energetically not in the ground state as the individual magnets would rather align in a long stick with their dipole along the stick's axis. However, without any external field, the pattern is metastable. To ensure mechanical stability even inside the external field, the magnets are glued with epoxy into a sample holder.

The experiments can be captured by a camera not shown in the schematic images. It is mounted at the sample holder giving a top view of the probe chamber. Furthermore, the pattern used in most experiments was one consisting of a few unit cells. Only seven full unit cells were accessible. The probe particle is placed in the center to

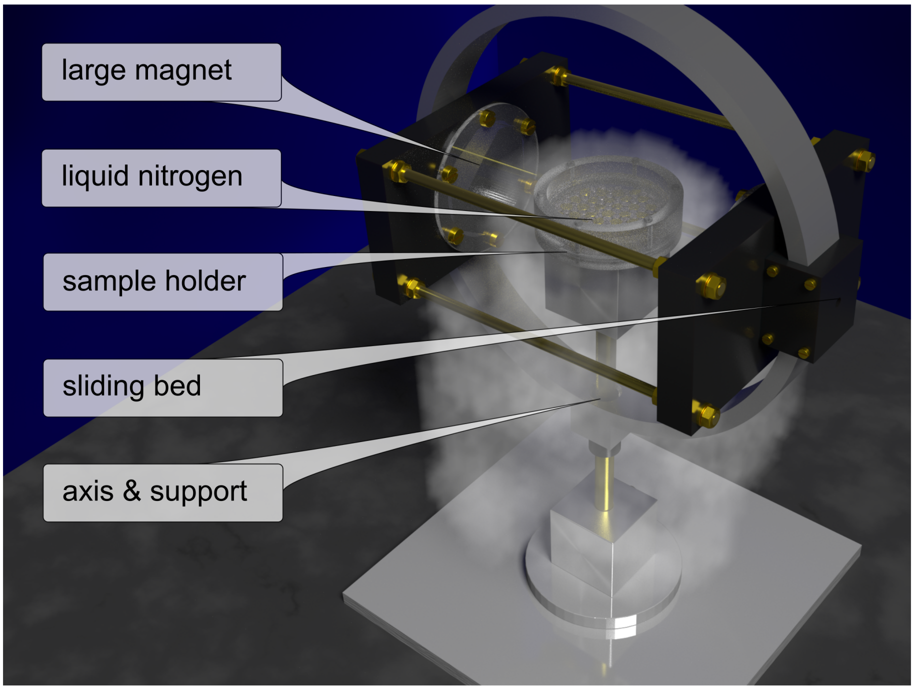

Figure 4.1: Schematic 3D representation of the goniometer. The large magnets producing the external field sit in a sled that can rotate along an aluminium ring. The transparent probe chamber above the sample holder is filled with liquid nitrogen to cool the superconductors. The sliding bed and the bearing at the supporting axis allow the external field to point in almost all directions. Only the areas close to the poles have to be omitted due to the bearing of the ring.

ensure approximate periodicity in all directions. The external magnets are turned slowly around the probe, such that the particles can follow the potential adiabatically.

Data of the octupole trajectories are obtained from the digital videos using manual tracking procedures.

4.1.2 Probe chamber

In the center of the goniometer, above the magnetic pattern, a small chamber is placed as seen in figure 4.2. Its main purpose is to contain the probe particles and the liquid nitrogen, used to cool the system to 77 K. The bottom is a plane, transparent disc. On top of this disk a ring with a height of 15 mm is glued to prevent leaks.

To ensure the universal height, some transparent spacers are placed in between the pattern and the probe chamber. The heat transfer should be minimized to avoid boiling of the liquid nitrogen. Therefore the spacers are rings, only touching the

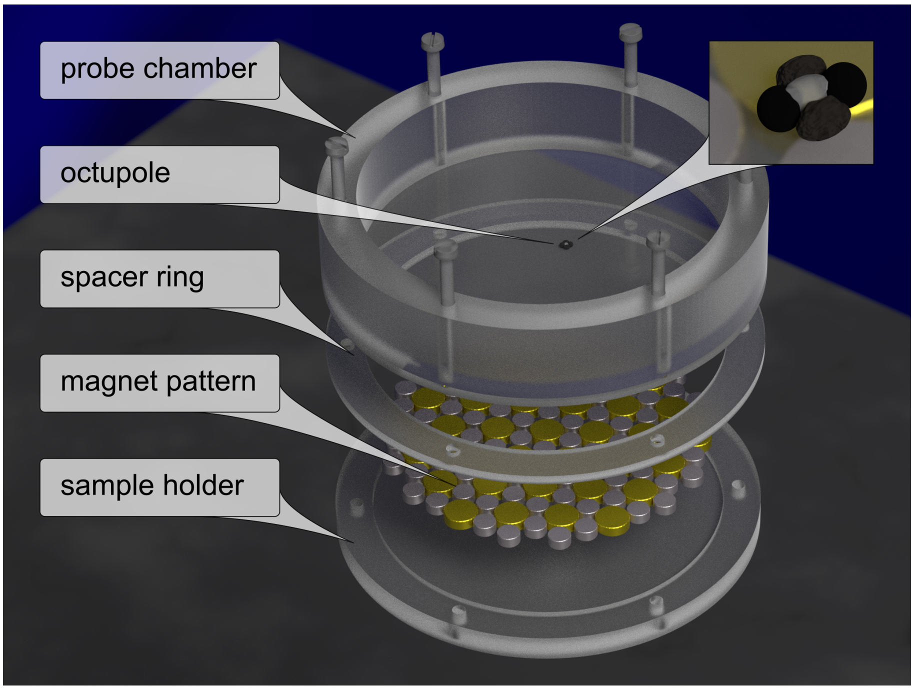

Figure 4.2: Schematic 3D representation of the probe chamber and adjacent parts sitting in the center of the goniometer shown in figure 4.1. On the bottom plate of the probe chamber, the octupole is placed. The inset shows the octupole consisting of two superconducting spheres, two deformed magnetite-wax-spheres and glue in the center. The spacer adjusts the distance to the pattern to guarantee the universal height. The magnetic pattern consists of individual magnets magnetized up (gold) and down (silver) respectively. The magnets are glued into a sample holder for mechanical stability.

---

outside of the probe chamber and leaving an isolating gap of air in between the surface of the pattern and the probe chamber.

Before placing the probe particles, the chamber is filled with liquid nitrogen until the boiling stops and disturbing convections in the fluid cease.

4.1.3 Octupole particles

To assemble locked octupoles, two paramagnetic and two diamagnetic particles of similar susceptibility are needed. The range of susceptibilities of diamagnets is limited. The minimal diamagnetic susceptibility is $\chi_{\text{superconductor}} = -1$ and hence a high temperature yttrium barium copper oxide (YBCO) superconductor is chosen. YBCO is a type-II-superconductor, therefore its susceptibility depends on both, temperature and external field. The field strength in the goniometer is 45 mT and the temperature is that of liquid nitrogen. The susceptibility can be estimated

Name	3:1	6:1	10:1	20:1
Wax in g	0.502	0.500	0.501	0.503
Magnetite in g	0.106	0.080	0.051	0.027

Table 4.2: Different mixtures of bee's wax and magnetite used in the experiments to form paramagnetic spheres. The name refers to the approximate mass ratio.

around $\chi_{\mathrm{YCBO}} \approx -0.8$ (Chen *et al.*, 1990) in this setup. The forces are calculated using the effective susceptibility taking the geometry of the spherical particles that build up the octupole, into account. For a sphere this yields:

$$\chi^{\mathrm{eff}} = \frac{\chi}{1 + \chi\frac{1}{3}} \tag{4.1}$$

These effective values have to be balanced in order to build an octupole with vanishing dipolar contributions. With $\chi^{\mathrm{eff}}_{\mathrm{YCBO}} \approx -1.1$ the paramagnetic material should have $\chi^{\mathrm{eff}}_{\mathrm{paramagnet}} \approx +1.1$ and therefore $\chi_{\mathrm{paramagnet}} \approx +1.7$.

To get a fitting paramagnetic material, magnetite powder from Sigma-Aldrich (Sigma-Aldrich, 2019) is mixed with non magnetic bees' wax by melting the wax and stirring until the wax/magnetite blend solidifies. The susceptibility of magnetite is in the range of $\chi_{\mathrm{magnetite}} \approx 1 - 5.6$ (Hunt *et al.*, 1995). A volume ratio of about $^5/_1$ wax to magnetite should therefore give results in the right order of magnitude. Taking the different densities ($\rho_{\mathrm{magnetite}} \approx 5\,\mathrm{kg\,l^{-1}}$) into account, this crude estimation gives a mass factor of about $^1/_1$. However, first experiments showed, that a lower percentage of magnetite is working better. To find an octupole, where para- and diamagnetic contributions are balanced, the percentage of magnetite is varied and different samples, summarized in table 4.2, are produced. The susceptibility of this composite wax-magnetite material was measured for the 3:1 wax-magnetite mixture in a magnetometer, using a spherical sample holder of diameter 5 mm. The result itself shows a small hysteresis. As only small fields are used, the hysteresis is neglected. A crude fit gives an effective susceptibility of $\chi^{\mathrm{eff}}_{3:1\ \mathrm{mixture}}(3{:}1) = 0.4$ in this approximation.

The superconducting spheres have a diameter of 1 mm. Spheres of the magnetite material of the same diameters are formed by rolling small amounts of the soft material between two glass slides using steel spheres of the same diameter as spacers to guarantee a compatibility of the sizes.

In a final step, two superconducting spheres and two paramagnetic magnetite-wax spheres are glued together in a lucky clover arrangement. Easiest handling is archived, when the superconductors are glued permanently and pressing the plastic wax material on both sides of this doublet as shown in the inset of figure 4.2. This leads to a slight deformation of the magnetite spheres.

The octupole particles are aligned at different angles γ towards the external field directions before placing them into the liquid nitrogen. Therefore, the external field direction is frozen into the superconductors at the specific angle of γ. Changing the locking angle during a measurement is possible by rotating the octupole with tweezers and holding them until the flux quanta relax to the new field direction after a couple of seconds.

The locking was examined on both, an empty sample and a C_6 pattern. The octupoles followed the external field in both cases such that after a full rotation of the external field along the equator of $\mathcal{C}$, the octupoles end with the same locking angles. This behaviour did not depend on the magnetite concentration in the range described in table 4.2.

The locking works only if the external field is not changing its precession angle θ. Changing θ during a $\mathcal{C}$-loop would lead to an erected octupole not laying flat on the probe chamber any more. Furthermore, only fields close to the equator result in reliable locking as the horizontal fraction of the external field decreases closer to the poles.

4.1.4 Precessing external fields

The paths of several octupoles as described in section 4.1.3 with varying paramagnetic strength and locking angles were recorded, tracked and analysed. The range of materials is analogue to the list of mixtures shown in table 4.2. Locking angles were varied in steps of 15°, the error is of similar magnitude. The magnetic field was only rotated along the equator. A constant tapping on the sample holder was applied to prevent sticking of the probe particles to the probe chamber.

Most of the octupoles run in a circle around one of the golden magnets. Therefore, comparison to paramagnetic and diamagnetic probe particles is necessary. This was done using single paramagnetic particles, single superconducting spheres, doublets of two diamagnets or two paramagnets and a fake octupole consisting of two superconductors and two non-magnetic wax spheres. The fake octupole shows the same hydrodynamic interaction and differs only in magnetite content, making it easily comparable with the octupoles.

The orientation, as well as the change of the external field for composite particles containing more than one superconductor can be extracted from the videos by tracking both superconductors individually. At the beginning of each video, the direction of the external field was indicated by a cord crossing the cameras view. The cord spans perpendicular to the external field.

4.2 Results for locked octupoles

Locked octupoles of different strength and dipole particles were studied with a precessing field in the equator of $\mathcal{C}$, as described in section 4.1.4. The results for some of them are shown in figure 4.3.

Stable paths similar to theoretically predicted locked octupole paths were obtained with the 10:1 mixture of wax and magnetite. The corresponding octupoles are named OP10 in the plots. The paths of octupoles with lower magnetite concentration (20:1) were more unstable and behaved more similar to a diamagnetic single particle. Higher concentrations led to a behaviour close to those of paramagnetic dipole particles. In the case of a 6:1 mixture, the resulting paths were still quite unstable. The following results are presented for the 10:1 mixture (see table 4.2).

The two different path shapes, the flower and the star, described in section 3.3 were found. The tips of the star are not detectable due to large noise, generated by the boiling liquid nitrogen. An example of a star is shown in the upper left of figure 4.3. The bottom left of this figure shows a segment of a flower path, where the octupole encircles the central golden magnet with a large radius and without ever getting close to the magnet itself. The agreement of the experimental path shapes with the theoretical paths is quite good, the locking angles however do not exactly fit the expectations. Nevertheless, uncertainties in adjusting the locking angles are large enough to cover the disagreement. Furthermore, the balance of susceptibilities might not be perfect. Composite particles with unbalanced effective susceptibilities, thus octupoles with a non-vanishing dipole character, in simulation show path shapes more similar to pure paramagnets or diamagnets with slight deformations. The experimental data clearly deviates from dipole paths.

As the star shaped path is effectively reduced to a circle in most cases (compare figure 4.3 upper right), the speed throughout the path has to be studied to see the main difference to a dipole particle. The paths in figure 4.3 are coloured according to

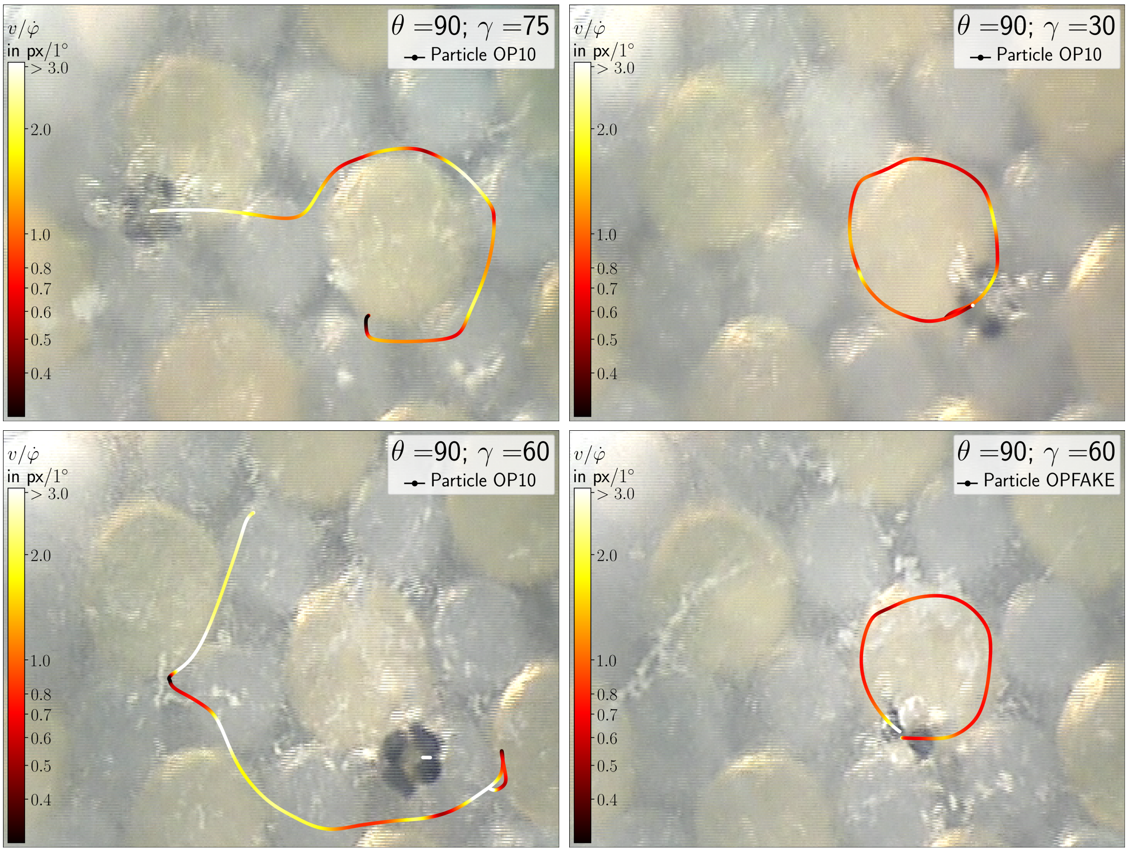

Figure 4.3: The experimental paths for octupoles (OP10) with a 10:1 mixture of wax and magnetite in the paramagnetic spheres and a fake octupole (OPFAKE) having no magnetite content in the wax spheres. The paths are coloured with their speed relative to the change of the magnetic field. A clear correlation between the position and speed can be seen for the octupoles (**upper row** and **lower left**). The octupole with $\gamma = 75°$ (**top left**) shows a path with clear waiting positions at the interstitials. The octupole $\gamma = 60°$ (**bottom left**) moves on a segment of a flower path, encircling the center magnet. The fake octupole (**bottom right**) shows the same behaviour as diamagnetic spheres. The background images are taken from the respective videos, showing the pattern and the probe particles at the end of the tracked path.

their current speed, normalized by the change of the external field. The normalization was necessary to adapt for different driving speeds throughout one, or in between different data sets. The data of one exemplary octupole is shown in figure 4.4. Clear minima separated by quite high maxima can be found. The minima correspond to the positions the tips of the stars are located and are in good agreement with the pattern (shown in the background of each plot in figure 4.3). The maxima are the ratchet jumps of one tip-position to another.

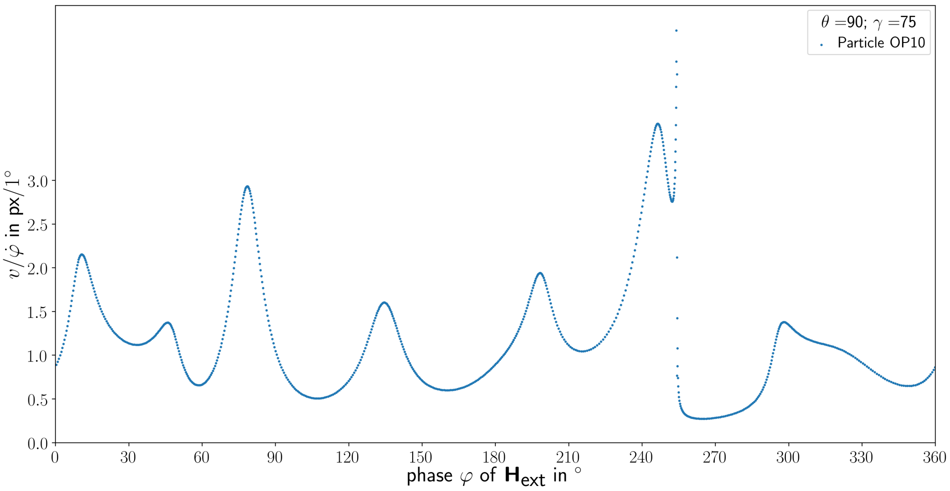

Figure 4.4: Measured speed of a locked octupole (OP10, $\gamma = 75°$) relative to the external field change. Six minima and six maxima, with the maxima corresponding to the ratchet transitions, are visible. The path data in the action space of this measurement is shown in the upper left of figure 4.3.

The dipole composite particles show a different behaviour where either no significant change in speed can be detected, as seen in the example in the bottom right of figure 4.3, or no correlation to the external field's phase or the position can be detected. This might lead to more than six minima or maxima.

Furthermore, the alignment of the external field's phase to the loop's phase, assigned to the probe particle's position in one loop, is quite characterizing the composite particle types. In the case of dipole particles, this phase is independent of e.g. the locking angle and their loops, hence their paths in $\mathcal{A}$ are quite stable. Paramagnets and diamagnets sit on opposing positions above the golden, central magnet, aligned with the external field's direction. In the case of locked octupoles, this position can change with the locking γ, as shown in section 3.3. The experimental data of the loop's phase is colour coded in figure 4.5. For an octupole with locking angle of $\gamma = 30°$ (left of figure 4.5), the starting position differs strongly from the positions of dia- or paramagnets like it can be seen for the fake octupole shown on the right side of figure 4.5. Neither path shape nor phase changes dramatically with the locking angle of the fake octupole.

The stability of the observed paths depends strongly on the used probe particle types. Whereas all types of dipole particles followed their tracks repeatable and almost

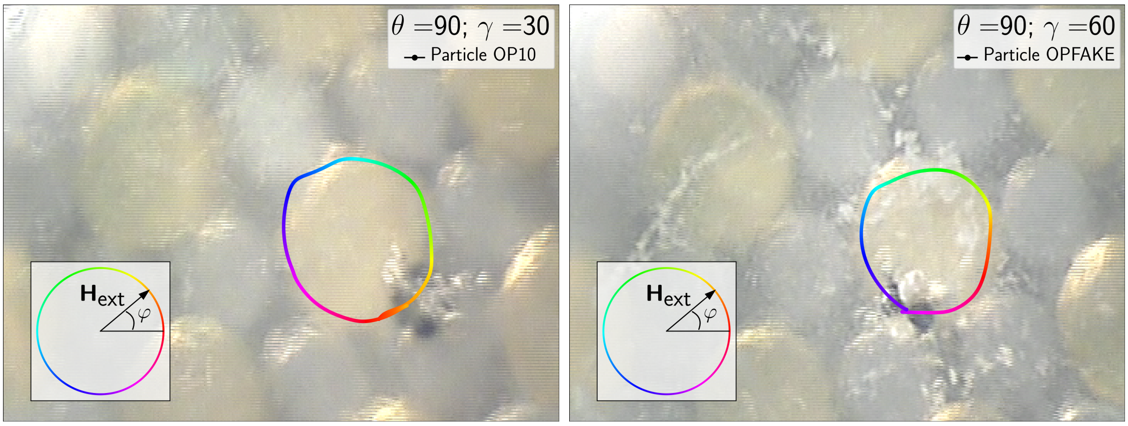

Figure 4.5: left: The experimental paths for an octupole (OP10) with a 10:1 mixture in the paramagnetic spheres and **right:** a fake octupole (OPFAKE), having no magnetite content in the wax spheres. The paths are coloured according to the phase of the external field rendering this position. The fake octupole (right) behaves exactly like a diamagnet, the octupole (left) with $\gamma = 30°$ has a loop's phase differing about $\pi/3$ from a dipole particle.

independent on the rotation speed of the external, driving field, the octupoles show different paths depending strongly on the driving speed. This is not unexpected, as the simulation showed a great impact of ratchet transitions for locked octupoles. The octupoles rather easily escaped from their starting unit cell like it can be seen in the top left octupole in figures 4.3. Generally the octupoles invaded deeper into the interstitial regions, the area outside the large magnet, than dipole particles. They even entered the space in between the smaller magnets, that is not accessible to any dipole particle at an arbitrary external field.

In conclusion, the observed octupoles show the different path shapes predicted by the simulation data for locked octupoles, a higher instability than dipole particles, different phases inside one loop in action space for different locking angles, and a clearly non-uniform speed throughout one field $\mathcal{C}$-loop. This gives reasons that the composite particles, built from type-II-superconductors and magnetite-wax-spheres in the right ratio of magnetite to wax, indeed show the behaviour of locked octupoles as predicted by the simulations.

5 Conclusion

In this thesis, the topological protected transport of induced magnetic octupoles on a magnetic pattern was studied. The position in the 2D action space and the orientation of an octupole are three degrees of freedom. Octupoles that were free to rotate, free octupoles, show a complex topology of paths, when subjected to an external field $\mathcal{C}$-loop. On patterns with C_6 symmetry, the path topology was found to be equivalent to saddle points of a single particle potential. Octupoles without this degree of freedom, locked octupoles, show some interesting behaviour in polar orbital fields and were studied in experiments and in simulation. Several sharp transitions were found in the systems. Deeper insights and possible explanations could be presented by observing the transitions under varying parameters.

5.1 Summary of particle types and their behaviour

The two types of studied particles, free and locked octupoles, show a quite different behaviour when subjected to an external, driving field and placed on a magnetic pattern. The trajectories of both particle types, subjected to different driving field $\mathcal{C}$-loops, were retrieved by simulations. Locked octupoles were further studied experimentally.

The simulation results of free octupoles on a C_6 pattern show two different loop types. For a precessing field close to the poles of $\mathcal{C}$, trivial loops in action space, that can be contracted to a point, exist. Those basin loops grow in size until the octupoles can not follow them any more. A topological transition happens close to the equator of $\mathcal{C}$, leading to a non-trivial double-triangle loop around the interstitials. On such double-triangle loops the octupoles move around an interstitial point twice per external field $\mathcal{C}$-loop in the direction opposing the direction of the driving field. The interstitial point itself can not be reached by the octupoles. The orientation rotates by π during such $\mathcal{C}$-loops. The path is shaped like a triangle at the equator.

Each segment splits into two for field $\mathcal{C}$-loops that deviate slightly from the equator of $\mathcal{C}$ giving rise to the double-triangle shape.

The transition from basin loops to double-triangle loops is better understood by examining the system with varying pattern symmetries. A pattern with a symmetry slightly varying from a perfect C_6 pattern shows a third loop type, a handle loop occurring at the transition from basin loops to double-triangle loops. The handle loop originates from segments of the basin loops of different basins. The basin loops grow in size with larger precession angles θ until parts of different basin loops connect to form one large triangle around the interstitial, the handle loop. At each corner of this loop the octupoles run in a small handle, as they try to follow the basin loop until a ratchet leads them to the next segment of an adjacent basin. A second transition transforms the handle loop into a double-triangle loop: the former basin loop segments grow even further in size until the ratchets connecting them cross on the other side of the interstitial point, leading to a free octupole effectively running twice around the interstitial. The closer the pattern symmetry gets to a S_6 pattern the broader is the range of precession angles where this handle loop is found. For a pure S_6 case, the handles of the handle loop vanish. One large attractor loop leads the octupoles around the remaining interstitial. The size of this loop decreases with larger precession angles until the attractor loop is contracted to a point and only one rotating octupole remains per unit cell.

This point of view further explains the speed of the free octupoles throughout one cycle. The high velocities found on the inner segments of the non-trivial double-triangle loops are inherited from the ratchet transitions connecting the stable parts of the handle loop. By looking at other symmetry cases, deep insight into the transition of the two topologically distinct loop types, found at the C_6 level is gained.

It was further shown that two free octupoles, sitting in one unit cell, can be exchanged with a complex driving $\mathcal{C}$-loop. This exchanges are generators of a braiding group, shown to be a subgroup of the B_3. By taking three free octupoles, real braiding is possible, giving rise to another field where topology is applied in physics, as described in the introduction. With strings attached to the octupoles, the state after winding one octupole around the other is topologically different. This is a particle model of the idea to use non-abelian anyons in quantum computation. Braiding in 2D is of course possible for all types of particles, with attached virtual or real strings. The basic and important difference is, that two identical particles are manipulated by the external field $\mathcal{C}$-loop that allows for a winding around each other. The possibility to braid with free octupoles makes them a fascinating analogue to anyonic quasi-particles used in quantum computation.

When enslaving the rotational degree of freedom to the external field, a second type of octupole, the locked octupole, is gained. The path behaviour received from simulation data can best be understood by comparing segments of paths of locked octupoles with segments of paths of free octupoles. The minima of free octupoles are energetically more favourable due to their extra degree of freedom. Hence, the locked octupoles follow those positions until their orientation makes the position unfavourable and a ratchet brings them to the next stable position.

The basic simulated paths of locked octupoles were found to have the shape of a star and a flower. Both, the star loop and the flower loop lead the octupoles once around a centred I0 region. The star loop excludes most of the basins' area. The tips of the star are connected with ratchets. Depending on the location of the adiabatic segment, two chiralities exist. An octupole on a flower loop encircles a larger area including most of the basins' area. At a certain precessing field, it depends on the locking angle γ of the locked octupole, which path it will follow. For precession angles close to the poles of $\mathcal{C}$, both types converge into each other. Observing the behaviour for smaller precession angles therefore helps to understand the different path types of octupoles with different locking angles at a precessing field close to the equator of $\mathcal{C}$.

A very interesting observation was made for polar orbiting field $\mathcal{C}$-loops. Placing locked octupoles on one fixed point in the action space leads to at least six different final locations after one sorting $\mathcal{C}$-loop. The outcome depends on the locking angle γ of the octupoles and the azimuthal angle φ of the driving field. Combining such $\mathcal{C}$-loops might be an interesting application for sorting locked octupoles in a robust way.

The locked octupoles were further studied in experiments showing the principle structures predicted from the simulations. Although the balance of the materials involved in building these complex composite particles is not perfect, clear signs indicate that the experimental locked octupoles do not behave like pure dipolar particles. Both theoretically predicted path shapes, the flower and the star, could be observed experimentally. The speed throughout one loop shows a ratchet type transition and some locked octupoles start at a different position at the same external field, as predicted for locked octupoles with different locking angles. The created composite particles, made from type-II-superconductors and magnetite-wax-spheres are therefore assumed to be locked octupoles. The flux quanta of the type-II-superconductors guaranteed the locking of the octupoles' rotation to the external field direction.

5.2 Outlook

The experiments show reasonable agreement with theoretical locked octupoles. Further experiments should be done to proof the agreement using different concentrations of magnetite-wax spheres. A larger pattern, containing more unit cells, could help to improve the paths stability and to study the sorting $\mathcal{C}$-loops described in the simulations.

A next step would be to create free octupoles. In the same system, this could be archived by pyrolytic graphite in wax, although the relevant forces could be orders to small to compete with noise. Löhr *et al.* (2016) used a colloidal microscopic model for the experiments on paramagnets and diamagnets. By filling the sample with a ferrofluid, a non-magnetic colloidal particle acts as a hole in the highly paramagnetic liquid and is therefore an effective diamagnet of high susceptibility. In this setup, free octupoles could be created by glueing two paramagnetic colloids and two non-magnetic colloids in a lucky clover arrangement. The glueing could be archived by using complementary DNA strands.

A Programs in Python

A.1 Version, packages, and scripts

All the simulations and the data processing was done in the scripting language python (version 3.6). To speed up the simulations, the `jitclass` of `numba` was used for several classes, which compiles python before running it. The package `numpy` was used for most calculations and data handling. Plotting was done with `mathplotlib.pyplot`. All scripts are build up from scratch.

The simulations are Brownian single particle simulations, meaning there is no interaction between two particles of any type. The randomness of the Brownian motion, as well as step size dt and speed of the introduced external field are adjusted to reduce numerical problems in the data and ensure adiabatic transport and still having a reasonable computation time for each simulation. The particles follow the potential minima adiabatically if the physics allows for it, leading to reproducible results. Each time step is executed as follows:

$$\boldsymbol{x}_{\mathrm{i}+1} = \boldsymbol{x}_{\mathrm{i}} + \boldsymbol{F}_{\mathrm{ext}}\,\mathrm{d}t + \boldsymbol{f} \tag{A.1}$$

with $\boldsymbol{F}_{\mathrm{ext}}$ being the external force on the particle and $\boldsymbol{f}$ a scalable random force.

The most important scripts are mentioned and shortly described here:

potential.py provides mainly the class `OctupolePotential()`. This class is the backbone of all the calculations. Based on the external field this class gives the potential and forces of a free, as well as a locked octupole, or the simple gradient of the paramagnetic, universal potential U. The class is optimized as a `jitclass`. The python file furthermore provides some functions to find minima of the octupole potential.

timestep.py introduces the jitclass `timestep()`, as well as classes for all particle types. With `timestep()` one can either propagate one particle for one step or simulate a full loop of some given external field. It uses some constants for step size and for the strength of the random Brownian contribution. The particle classes provide simple functions as getting or changing the current position and orientation. The main difference of these classes is the way the force acting on them is defined. Only the `Saddleseeker()` class could not be optimized as a `jitclass`, because it is not really simulating a force acting on the particle, but searches for the closest saddle point by finding the roots of the potential. This root finding is done with `fsolve` from `scipy.optimize`. It needs an unoptimized `timestep()` class to run. Apart from these classes some functions to generate the external magnetic field are provided by this script.

plotting.py provides all functions often used in the plots. 3D plots are implemented with the package `mpl_toolkits.mplot3d`.

animation3x.py is the script running a live simulation of a given set of particles. It simulates and animates the paths of all particles to a given external field loop and gives the option to save videos or path data.

plotpath_*.py are files used to make action space plots out of saved path data, depending on the given data structure several of these files exist.

other files are scripts for individual problems and need no further description.

All programms were run on a Windows 10 computer using the Spyder 3.2.8 environment for debugging and data analysis. Paths data is saved as `*.dat` files.

A.2 Particle forces

The forces of the individual particles are derived as follows

Paramagnet The force is the gradient of the universal potential U (equation 2.5), as a paramagnet tries to maximize the potential.

$$\boldsymbol{F}_{\mathrm{p}} = \nabla U \tag{A.2}$$

Diamagnet The force is, except for the inverse direction, the same as for a paramagnet.

$$\boldsymbol{F}_{\mathrm{d}} = -\nabla U \tag{A.3}$$

Free octupole Using equation 2.15 and taking the 2D gradient gives the force on a free octupole. The constant factor r^2 of equation 2.15 is set to 1 for simplicity.

$$\boldsymbol{F}_{\text{free}} = -\nabla\sqrt{\left(U_{xx} - U_{yy}\right)^2 + 4U_{xy}^2} \tag{A.4}$$

Locked octupole According to equation 2.19 the forces of the four dia- or paramagnetic particles are summed up. To introduce the possibility of changing the ratio of the distance or χ of the two particle types two further variables are introduced. With $r_p = r + \delta r$ and $r_d = r - \delta r$ as well as $\chi_p = 1 - \delta\chi$ and $\chi_d = -1 - \delta\chi$.

$$\begin{aligned} \boldsymbol{F}_{\text{locked}} = &\quad (1-\delta\chi)\left(\boldsymbol{F}_{\text{p}}(\boldsymbol{x} + (r+\delta r)\hat{\boldsymbol{e}}_{\text{p}}) + \boldsymbol{F}_{\text{p}}(\boldsymbol{x} - (r+\delta r)\hat{\boldsymbol{e}}_{\text{p}})\right) && \text{(A.5)} \\ - &\quad (1+\delta\chi)\left(\boldsymbol{F}_{\text{p}}(\boldsymbol{x} + (r-\delta r)\hat{\boldsymbol{e}}_{\text{d}}) + \boldsymbol{F}_{\text{p}}(\boldsymbol{x} - (r-\delta r)\hat{\boldsymbol{e}}_{\text{d}})\right) && \text{(A.6)} \end{aligned}$$

To make the force comparable to $\boldsymbol{F}_{\text{free}}$ it was then multiplied with a factor of $1/r^2$, that was omitted in equation A.4.

Saddle point No force was assigned for a particle going to a real saddle point. The position was calculated by finding the roots of U and using the root with semi-definite Hessian matrix.

The orientation of the free octupoles was defined by taking the eigenvectors of $\nabla\nabla U$ and orienting the paramagnets along the eigenvector belonging to the bigger eigenvalue. The same holds for the saddle point orientation. All other particles were oriented with some relative angle γ to the projection of the external field $\boldsymbol{H}_{\text{ext}}$, which gives no further information for a para- or diamagnet, but counts for the fact, that the locked octupoles are enslaved to the external field.

List of Symbols and Abbreviations

Symbol	**Description**	**Unit**
$\boldsymbol{H}$	Magnetic field vector, 3D	$\mathrm{A\,m^{-1}}$
$\boldsymbol{H}_{\mathrm{ext}}$	External, driving field	$\mathrm{A\,m^{-1}}$
θ	Inclination of external magnetic field $\boldsymbol{H}_{\mathrm{ext}}$	$^\circ$
φ	Azimuth of external magnetic field $\boldsymbol{H}_{\mathrm{ext}}$	$^\circ$
$\boldsymbol{H}_{\mathrm{p}}$	Pattern field	$\mathrm{A\,m^{-1}}$
a	Lattice constant of the pattern	m
$\boldsymbol{a}_1$, $\boldsymbol{a}_2$	primitive lattice vectors of the pattern	
ϕ	Symmetry parameter specifying the pattern	1
$\boldsymbol{M}$	Magnetization	$\mathrm{A\,m^{-1}}$
μ_0	Vacuum permeability, constant	$4\pi \times 10^{-7}\,\frac{\mathrm{V\,s}}{\mathrm{A\,m}}$
χ	Magnetic susceptibility	1
U	Universal potential	$\mathrm{A^2\,m^{-2}}$
W	Potential of free octupoles	$\mathrm{J\,m^{-3}}$
$\boldsymbol{F}$	Force	N
Octupole parameters		
r	Size of an octupole	m
Φ	Orientation of an octupole	$^\circ$
γ	Locking angle between diamagnets and $\boldsymbol{H}_{\mathrm{ext}}$	$^\circ$
Mathematical symbols		
$\underline{\underline{\boldsymbol{R}}}$	2D rotation matrix	
∇	2D Nabla operator	
$\boldsymbol{v}, v$	Some vector, and its magnitude	
$\hat{\boldsymbol{e}}$	2D unit vector	
$\underline{\underline{\boldsymbol{A}}} : \underline{\underline{\boldsymbol{B}}}$	Contraction of the matrices $\underline{\underline{\boldsymbol{A}}}$ and $\underline{\underline{\boldsymbol{B}}}$	

List of Figures

2.1 Geometrical objects having a different genus 14

2.2 Unit cell of six fold pattern represented on a torus 15

2.3 Controlspace, action space and manifold of a C_6 pattern (Löhr *et al.*, 2017) 17

2.4 Non-trivial behaviour of saddle points for driving $\mathcal{C}$-loops in the tropics 18

2.5 Behaviour of two particles being exchanged in 3D and 2D 19

2.6 Basic concepts of braiding particles and the braiding group 21

2.7 Induced octupole, schematically 23

3.1 Sixfold pattern with potential landscape for a free octupole 30

3.2 Free octupole paths for precessing $\mathcal{C}$-loops outside the tropics, basin loops 32

3.3 Free octupole paths for precessing $\mathcal{C}$-loops in the tropics, non-trivial interstitial loops 34

3.4 Velocities of free octupoles throughout precessing $\mathcal{C}$-loops 35

3.5 Transition of paths characteristics, coloured according to octupole speed 36

3.6 Free octupole paths for polar orbital $\mathcal{C}$-loops 39

3.7 Comparison of free octupoles paths with saddle point positions 40

3.8 Potential landscape and unit cell for different three fold symmetries . 42

3.9 Free octupole paths in different symmetries 43

3.10 Phase diagram of paths characteristics of free octupoles regarding symmetries ϕ and precession angles θ 46

3.11 Exchange $\mathcal{C}$-loops and the paths of both free octupoles 48

3.12 Braiding of three octupoles on a C_6 pattern 50

3.13 Locked octupole paths for different precession angles with locking angle $\gamma = 105°$ 54

3.14 Locked octupole paths for different locking angles at constant precession $\theta = 90°$ 55

3.15 Phase diagram for path characteristics of locked octupoles regarding locking angle γ and precession angle θ 57
3.16 Phase diagram of sorting behaviour of locked octupoles in polar orbiting fields regarding locking angle γ and azimuthal φ 59

4.1 3D representation of the goniometer 63
4.2 3D representation of the probe chamber, the magnetic pattern, and the octupole 64
4.3 Experimental paths of octupoles and a fake octupole with their relative speed 68
4.4 Experimental speed of a octupole during one field $\mathcal{C}$-loop 69
4.5 Experimental paths of an octupoles and a fake octupole with their relative phase 70

Bibliography

Brandt, E. H. 1990 Rigid levitation and suspension of high temperature superconductors by magnets. *American Journal of Physics* **58** (1), 43–49.

Chen, D.-X., Sanchez, A., Puig, T., Martinez, L.M. & Muñoz, J.S. 1990 Ac susceptibility of grains and matrix for high-tc superconductors. *Physica C: Superconductivity* **168** (5), 652 – 667.

Devitt, Simon J., Munro, William J. & Nemoto, Kae 2013 Quantum error correction for beginners. *Reports on Progress in Physics* **76** (7), 076001.

Dufresne, Eric R. & Grier, David G. 1998 Optical tweezer arrays and optical substrates created with diffractive optics. *Review of Scientific Instruments* **69** (5), 1974–1977.

Hasan, M. Z. & Kane, C. L. 2010 Colloquium: Topological insulators. *Rev. Mod. Phys.* **82**, 3045–3067.

Hunt, Christopher P ., Moskowitz, Bruce M. & Banerjee, Subir K . 1995 *Rock Physics & Phase Relations: A Handbook of Physical Constants*, , vol. 3, chap. 3-14, pp. 189–204. American Geophysical Union.

Löhr, Johannes 2017 *Magnetically induced dynamics of mesoscopic colloidal systems*. PhD thesis, Universität Bayreuth.

Löhr, Johannes, de las Heras, Daniel, Jarosz, Adam, Urbaniak, Maciej, Stobiecki, Feliks, Tomita, Andreea, Huhnstock, Rico, Koch, Iris, Ehresmann, Arno, Holzinger, Dennis & Fischer, Thomas M. 2018 Colloidal topological insulators. *Communications Physics* **1** (1).

Löhr, Johannes, de las Heras, Daniel, Lönne, Michael, Bugase, Jonas, Jarosz, Adam, Urbaniak, Maciej, Stobiecki, Feliks, Tomita, Andreea, Huhnstock, Rico, Koch, Iris, Ehresmann, Arno, Holzinger, Dennis & Fischer, Thomas M. 2017 Lattice symmetries and the topologically protected transport of colloidal particles. *Soft Matter* **13** (29), 5044–5075.

Löhr, Johannes, Lönne, Michael, Ernst, Adrian, de las Heras, Daniel & Fischer, Thomas M. 2016 Topological protection of multiparticle dissipative transport. *Nature Communications* **7** (1).

Maier, Florian Johannes, Lachner, Thomas, Vilfan, Andrej, Tasci, T. Onur, Neeves, Keith B., Marr, David W. M. & Fischer, Thomas M. 2016 Non reciprocal skewed rolling of a colloidal wheel due to induced chirality. *Soft Matter* **12**, 9314–9320.

Martinez-Pedrero, Fernando & Tierno, Pietro 2015 Magnetic propulsion of self-assembled colloidal carpets: Efficient cargo transport via a conveyor-belt effect. *Phys. Rev. Applied* **3**, 051003.

Nash, Lisa M., Kleckner, Dustin, Read, Alismari, Vitelli, Vincenzo, Turner, Ari M. & Irvine, William T. M. 2015 Topological mechanics of gyroscopic metamaterials. *Proceedings of the National Academy of Sciences* **112** (47), 14495–14500.

Nayak, Chetan, Simon, Steven H., Stern, Ady, Freedman, Michael & Das Sarma, Sankar 2008 Non-Abelian anyons and topological quantum computation. *Reviews of Modern Physics* **80** (3), 1083–1159.

Rossi, Anna M. E. B., Bugase, Jonas & Fischer, Thomas M. 2017 Macroscopic floquet and topological crystalline steel and superconductor pump. *EPL (Europhysics Letters)* **119** (4), 40001.

Shor, P. W. 1994 Algorithms for quantum computation: discrete logarithms and factoring. In *Proceedings 35th Annual Symposium on Foundations of Computer Science*, pp. 124–134.

Sigma-Aldrich 2019 Sicherheitsdatenblatt gemäß Verordnung (EG) Nr. 1907/2006 zu Iron(II,III) oxide, Produktnummer 310069, Version 6.1.

Stern, Ady 2008 Anyons and the quantum Hall effect—A pedagogical review. *Annals of Physics* **323** (1), 204–249.

ZHU, QI-ZHONG & WU, BIAO 2015 Superfluidity of bose-einstein condensates in ultracold atomic gases. *Chinese Physics B* **24** (5), 050507.

Danksagung

Ich möchte all den Menschen danken, die mit zum Erfolg dieser Arbeit beigetragen haben, die mich in der Zeit der Masterarbeit begleitet haben und mir mit Rat und Tat zur Seite standen:

Meinem Betreuer **Thomas Fischer** für die vielen motivierenden Gespräche, inhaltlichen Diskussionen und der Freude an meinen Ergebnissen. Es war schön, dich als Betreuer zu haben!

Der ganzen **Arbeitsgruppe Experimentalphysik X** für viele schöne Stunden in unserem Kellerbüro mit viel Tee und Eiskaffee.

Adrian Ernst für die Unterstützung beim Programmieren.

Carmen Kerling für das Bereitstellen des Stickstoffs.

Klaus Oetter für Alles, was mechanisch gebaut werden musste und immer schnell und professionell erledigt wurde.

Reinhard Richter für die Magnetometermessung.

Der **Fachschaft MPI** für Kaffee und Süßigkeiten und für die vielen offenen Ohren.

Tobias Kreisel für Hilfe bei allem Administrativen und Fragen zur Prüfungsordnung.

Markus Hilt dafür, dass er mit mir den Kampf im CAMPUSonline Jungle bestritten hat.

Stefan Conrad für Diskussionen, Ratschläge, lange Telephonate und das Korrigieren der ersten Fassung.

Meinen Eltern **Monika und Dieter Lachner** dafür, dass sie immer hinter mir standen.

Meiner WG, der **B36** und meinen **Freunden**, die versucht haben, meine Arbeit mit Tassen, Tellern und Donuts zu verstehen und mir dadurch geholfen haben, selbst einen tieferen Einblick zu erlangen.

Und ganz besonders natürlich **Anna Rossi**, an deren Aufbau ich messen durfte, die mir stützend und beratend die ganze Zeit zur Seite stand, sich alle meine Probleme angehört hat, gute Ratschläge gibt, viele Kommas findet und einfach für mich da ist.

Erklärung

Hiermit erkläre ich, dass ich die vorliegende Arbeit selbstständig verfasst und keine anderen als die angegebenen Quellen und Hilfsmittel benutzt habe. Diese Arbeit wurde von mir bisher weder in gleicher noch in ähnlicher Form zur Erlangung eines akademischen Grades eingereicht.

Bayreuth, den 30. September 2019 ....
Thomas Lachner